

2009

Exploring Fundamental Turbulent Physics Using Direct Numerical Simulation

Michael A. Nilsson

University of Massachusetts - Amherst, mnilsson@student.umass.edu

Follow this and additional works at: <http://scholarworks.umass.edu/theses>

Nilsson, Michael A., "Exploring Fundamental Turbulent Physics Using Direct Numerical Simulation" (2009). *Masters Theses 1896 - February 2014*. Paper 259.
<http://scholarworks.umass.edu/theses/259>

This Open Access is brought to you for free and open access by the Dissertations and Theses at ScholarWorks@UMass Amherst. It has been accepted for inclusion in Masters Theses 1896 - February 2014 by an authorized administrator of ScholarWorks@UMass Amherst. For more information, please contact scholarworks@library.umass.edu.

**EXPLORING FUNDAMENTAL TURBULENT
PHYSICS USING DIRECT NUMERICAL SIMULATION**

A Thesis Presented

by

MICHAEL A NILSSON

Submitted to the Graduate School of the
University of Massachusetts Amherst in partial fulfillment
of the requirements for the degree of

MASTER OF SCIENCE

May 2009

Mechanical and Industrial Engineering

© Copyright by Michael A. Nilsson 2009

All Rights Reserved

**EXPLORING FUNDAMENTAL TURBULENT
PHYSICS USING DIRECT NUMERICAL SIMULATION**

A Thesis Presented

by

MICHAEL A NILSSON

Approved as to style and content by:

J. Blair Perot, Chair

Stephen de Bruyn Kops, Member

Yossi Chait, Member

Mario A. Rotea, Department Head
Mechanical and Industrial Engineering

ACKNOWLEDGMENTS

I would like to begin by thanking my family for their unwavering support, and to Christyne for her support and patience in this thesis endeavor. I would like to thank Professor Perot for his insight, guidance, patience, and direction as I endeavor deeper into the world of fluids and turbulence. Thanks to Jay Gadebusch for answering an initial unrelenting assault of questions when learning the art of code generation of fluids. Thanks to Dave Hebert, Michael Martell, Shivasubramanian Gopalakrishnan, Sandeep Menon, and Venkataramanan Subramanian for their wealth of knowledge of CFD and linux. Finally, thanks to Geoff Moss, Robert Daniello, Molly Mulligan, Kshitij Neroorkar, Dnyanesh Digraskar, Kaustubh Rao, and Raghuveer Sesha Vajapeyayajula for keeping the journey through graduate school fun.

ABSTRACT

EXPLORING FUNDAMENTAL TURBULENT PHYSICS USING DIRECT NUMERICAL SIMULATION

MAY 2009

MICHAEL A NILSSON

B.S.M.E., UNIVERSITY OF MASSACHUSETTS AMHERST

M.S.M.E., UNIVERSITY OF MASSACHUSETTS AMHERST

Directed by: Professor J. Blair Perot

It has been shown in many studies that turbulent flows are highly dependent on their initial conditions. This thesis explores turbulent flow using direct numerical simulation (DNS) in a variety of situations, and culminates in the development of physically realizable initial conditions. The reaction of isotropic homogeneous turbulent flow to the instantaneous insertion of a wall is investigated using two-point correlations. A model with which to predict the behavior of the two-point correlations is also proposed. The proposed model utilizes a reflection technique that with a linear operation, it accurately predicts the behavior of the non-linear two point correlations. The model works exceedingly well for correlations involving wall-perpendicular velocities, but does not predict correlations involving only wall-parallel velocities as well. A vorticity approach is covered, in an effort to highlight which parts of the correlation decomposition are important to the prediction of the correlations after wall imposition. The vorticity study also helps highlight why the proposed linear model predicts the flow. The impact of the initial conditions on axisymmetric contraction flow of turbulent flow is examined, and as a consequence new initial conditions are

developed based off of a physically realizable flow condition. The development of the new-initial conditions and the resulting fields are covered, as well as a study on the value of the turbulent decay exponent associated with decay of isotropic turbulent velocity fields.

TABLE OF CONTENTS

	Page
ACKNOWLEDGMENTS	iv
ABSTRACT	v
LIST OF FIGURES	viii
CHAPTER	
1. INTRODUCTION	1
1.1 Introduction.....	1
1.2 Assumptions.....	1
1.3 Direct Numerical Simulations.....	5
1.4 Initial Conditions	6
1.5 Two-Point Correlations.....	8
1.6 Application of Walls.....	10
1.7 Low Reynolds Number Flows	11
1.8 Decay Exponent.....	13
2. NUMERICAL METHODS	17
2.1 Overview.....	17
2.2 Meshing.....	20
2.2 Two-Point Correlations.....	22
2.3 Greens Method.....	25
2.4 Initial Condition Generation	28
3. RESULTS.....	32
3.1 Wall Insertion.....	32
3.2 Green's Method Validation.....	34
3.3 Two-Point Correlations.....	36
3.4 Vorticity	53
3.5 Low Reynolds Number Strain Flow	69
3.6 New Initial Conditions	73
3.7 Decay Exponent.....	81
4. CONCLUSIONS.....	87
REFERENCES	90

LIST OF FIGURES

Figure	Page
1 – 1: U-velocity of peak magnitude of 30m/s contours in an X-Y Slice through a 256 x 256 x 512 mesh turbulent isotropic velocity field.....	2
1 – 2: Idealized representation of a 3-D turbulent energy spectrum (black) with a -5/3 slope line (red). The energy spectrum tapers off to the inverse of the Kolmogorov lengthscale.....	4
1 – 3: k^2 low wave number spectrum turbulent decay exponent, n , versus the corresponding turbulent Reynolds number, Re_T	15
2 – 1: Example of velocity distribution and pressure distribution about each cell in the staggered mesh.....	21
2 – 2: A three-dimensional view of an R_{11} correlation using transparent iso-surfaces to show intensity values	23
2 – 3: A typical f-correlation of isotropic homogenous turbulence, in this case the R_{22} f-correlation (from 32^3 field).	24
2 – 4: Representation of how the code develops and calculates the Green method approach.....	27
2 – 5: A pictorial representation of the jet activation concept.....	30
3 – 1: Simulation domain showing where the boundary conditions are imposed (shaded sides).	33
3 – 2: Comparison of pressure fields. The left field is generated from the Greens method, and the right field is generated from the Navier-Stokes solver.....	35
3 – 3: f-correlations of the initial velocity fields.	36
3 – 4: R_{11} correlation looking at the r_x - r_z Plane at $r_y = 0$	38
3 – 5: r_x - r_z planar slice of R_{11} correlation at $r_y = 0$ (left), Center of R_{11} correlation zoomed in (right).....	40
3 – 6: A r_x - r_y planar slice of the R_{22} correlation field through $r_z = 0$	41

3 – 7: A r_x - r_y planar slice of the R_{22} correlation field through $r_z = 0$ after the imposition of walls.....	42
3 – 8: r_y - r_z plane of the R_{11} Correlation at $r_x = 0$ pre-wall (left), post-wall (right)	44
3 – 9: r_y - r_z plane at $r_x = 0$ of the R_{11} correlation's constitutive parts. The first part (left), second part (middle), and third part (right)	44
3 – 10: r_x - r_y Plane at $r_z = 0$ of the difference between the R_{22} before and after the insertion of the wall.....	45
3 – 11: R_{22} f-correlation with the difference between the two wall conditions plotted	46
3 – 12: R_{22} f-correlation with the mirrored and shifted R_{22} correlation plotted, and the resulting difference and actual R_{22} result after the wall	47
3 – 13: R_{22} f-correlation with the mirrored and shifted R_{22} correlation plotted, and the resulting difference and actual R_{22} result after the wall. The wall is 4 cell locations from the center of the correlation	48
3 – 14: R_{22} f-correlation with the mirrored and shifted R_{22} correlation plotted, and the resulting difference and actual R_{22} result after the wall. The wall is 6 cell locations from the center of the correlation	49
3 – 15: R_{11} g-correlation with the mirrored and shifted R_{11} correlation plotted, and the resulting difference and actual R_{11} result after the wall. The wall is 2 cell locations from the center of the correlation	50
3 – 16: Graphical representation of the reflection technique and the correlations it predicts	51
3 – 17: R_{12} correlation in 3-dimensions (left) and a r_x - r_y planar slice about $r_z = 0$ (right).....	52
3 – 18: R_{12} correlation after wall insertion, reflection model (left) and computed (right).....	52
3 – 19: Vorticity field calculation.....	54
3 – 20: Diagram of single vortex (black arrow) in a domain.....	57
3 – 21: The velocity associated with a vortex strength of 100 for different resolutions. Theoretical result (colored lines), computed result(circles with solid black lines)	58

3 – 22: Diagram representing the case of a planar sheet of vorticity (blue) in a domain.	60
3 – 23: Planar Velocities as a result of a vortex sheet.	61
3 – 24: Tube of vorticity results. A.) V-velocity along a line in the x -direction. B.) Velocity vectors showing both magnitude and direction.	62
3 – 25: Error resulting from different values of C in the calculation of σ .	63
3 – 26: Velocity comparison of the actual resulting velocity field and that generated from the vorticity.	64
3 – 27: Reflected, semi-periodic domain.	65
3 – 28: The v -velocity contributions from the vorticity beyond the wall (left image), and contributions of the vorticity to the existing side of the wall (right image). The wall is located at $Y = 0$.	67
3 – 29: Decomposition of the correlations. Clockwise, from top left, the RR correlation, the RL correlation, the LR correlation, the LL correlation. In each image, the wall is located at the top.	68
3 – 30: R_{11} , R_{22} , R_{33} , normalized by the initial kinetic energy versus non-dimensional time, St .	70
3 – 31: XY -Planar velocity averages of the u - and v -velocity fields in the z -direction.	72
3 – 32: Planar velocity averages of the v -velocity fields in the z -direction (solid), the correcting function (red dashed), and the resulting corrected profile (blue dashed).	73
3 – 33: Cross sections of velocity fields showing the u , v , and w velocity fields, from left to right, respectfully.	74
3 – 34: Turbulent Reynolds number (Re_t), Kinetic Energy (TKE), and Dissipation (ϵ) vs. time (in seconds).	75
3 – 35: Simplified diagram of flow field with cubes placed randomly inside.	77
3 – 36: Full field of u -velocity contours.	80
3 – 37: Resulting R22 Correlations, looking at a X - Z slice in the center of the correlation field.	81
3 – 38: Decay Exponent, n , vs Time (s) of various initial conditions decaying.	82

3 – 39: Kinetic Energy vs. Time of decaying flow (top); Dissipation vs. Time of decaying flow (bottom)	83
3 – 40: The decay exponent vs. time, showing the difference between the averaging schemes. The theoretical k^2 and k^4 limits for high Reynolds Number decay are shown by the fuchsia lines	84
3 – 41: The turbulent decay exponent vs. Turbulent Reynolds Number. The theoretical k^2 and k^4 limits for high Reynolds Number decay are shown by the fuchsia lines (1.2 is the bottom limit of the figure).....	85

CHAPTER 1

INTRODUCTION

1.1 Introduction

Turbulence is a phenomena that has intrigued people for years. It can be seen in many daily observable events, from atmospheric events, down to pouring a glass of water. However, despite years of study, turbulence remains a largely unsolved problem. Much effort and research has gone into developing a theory behind turbulence. While many methods and schools of thought have been developed, the ideas and concepts discussed in this thesis concern the direct simulation of turbulence using numerical methods, how turbulence reacts with the presence of a wall imposed on a very small timescale, low Reynolds number flow behavior, and the physically realizable development of turbulent initial conditions.

1.2 Assumptions

In the natural world, many different types of turbulent flows are witnessed and created. Due to the complexity of their nature, developing an understanding of every flow imaginable would be near impossible. A simpler and more manageable approach is to study a simple form of turbulence. For this thesis, the main area of focus deals with understanding homogeneous isotropic turbulence. A visualization of a turbulent field is shown in figure 1-1.

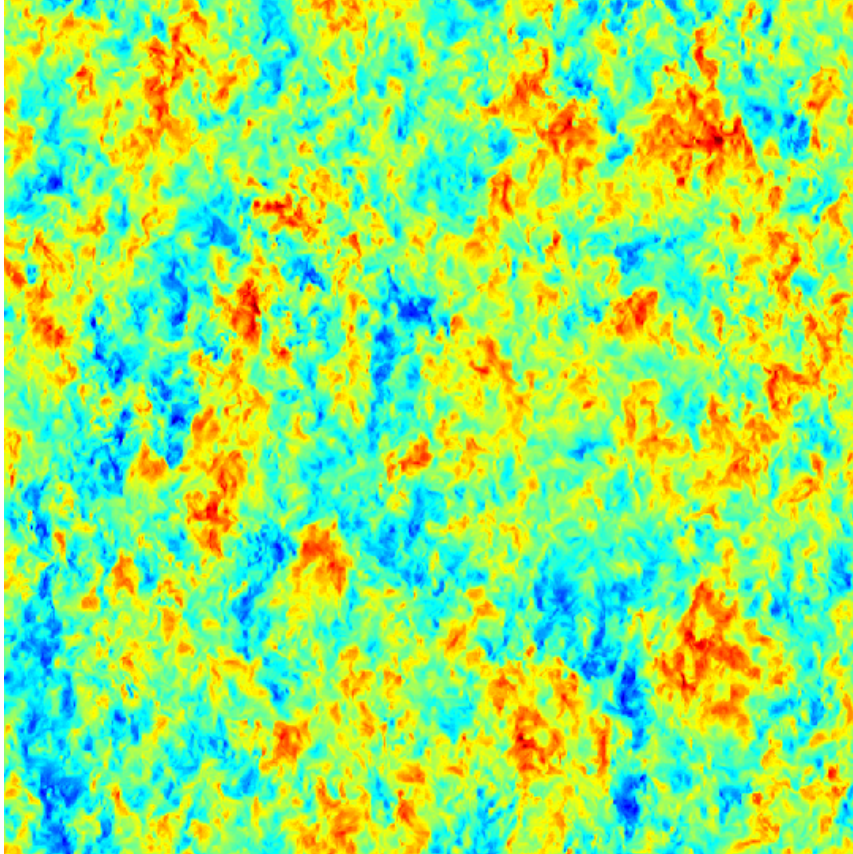


Figure 1-1: U-velocity of peak magnitude of 30m/s contours in an X-Y Slice through a 256 x 256 x 512 mesh turbulent isotropic velocity field.

Isotropic homogenous turbulence is one of the simplest types of turbulent flows for academic study. Much of turbulence theory is based on and derived from the study of this flow[1]. Isotropy is defined as being statistically similar in any direction. Homogenous turbulence means that fluctuating velocities in the field are statistically not a function of position. To be statistically homogeneous is to have any statistics be identical over any sampling of the domain, or a shift in position. It is relatively difficult to create experimental turbulent flows that are truly isotropic and homogenous, though wind tunnels approximate this condition reasonably well.

A main concept underlying turbulent flows is that there are multiple length scales and time scales involved. These multiple length and timescales are derived from

the concept that turbulence is comprised of many different eddies, and not just random motion. While seemingly random in nature, these varied eddies and their motion directly affect the motion of the fluid around it, and thus there can be considered structure to turbulence. This structure can be seen in the two-point correlations detailed later in this and subsequent chapters. If turbulence was characteristically random, the two-point correlations would be delta functions.

Generally, turbulent flows exist at high Reynolds numbers, which allow certain assumptions to be made designed to simplify the complexity that a turbulent flow exhibits. Many of the fundamental hypotheses that govern many models and understanding of turbulence were quantified by Kolmogorov, and outlined concisely by Pope[1]. Essentially, the result of applying the Kolmogorov hypotheses, is to reduce the complexity of the small scale energy dissipation, allowing for it to be considered statistically isotropic, and dependent only on the kinematic viscosity, ν , and the dissipation rate, ε . Furthermore, this theory assumes that only the small scale eddies are affected by the viscosity, and that energy transfer from large scales to smaller scales occurs with no real penalty either way. In three-dimensional turbulence, then energy transfer predominantly cascades from larger to smaller structures, and is assumed to be solely a function of the dissipation rate.

The idea of energy flowing from one length scale to another gives rise to the concept of a turbulent energy cascade. It is often desirable to examine the energy spectrum because it is a simpler than examining the energy in physical space. In creating either a velocity spectra or energy spectra from a standard space field of turbulence, the positional dependence of the velocity or energy is lost, thus creating a

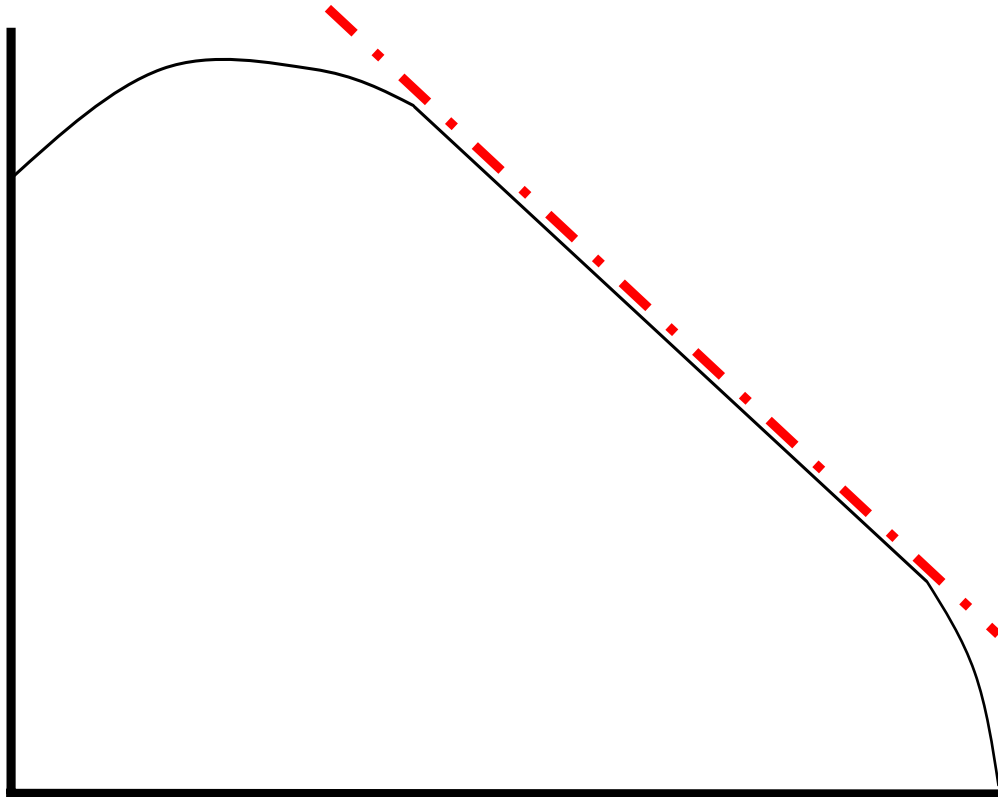


Figure 1 – 2: Idealized representation of a 3-D turbulent energy spectrum (black) with a $-5/3$ slope line (red). The energy spectrum tapers off to the inverse of the Kolmogorov lengthscale.

simpler description of the desired information. The energy of the system in Fourier space, in itself, leads to some key concepts in turbulence, such as quantification of the energy cascade and dissipation.

Figure 1-2 shows a typical energy spectrum of turbulent energy decay. The small wave numbers, on the left of the figure, contain the most energy, and represent the energy contained in the large eddies. The energy decays as the wave number increases, which describes the transfer of energy to smaller and smaller scales, down to the Kolmogorov length scale. For moderate Reynolds numbers, the energy tends to be less linear in the inertial subrange, and only a small portion of the spectra has a $-5/3$ slope.

1.3 Direct Numerical Simulations

Turbulent flow is chaotic, and therefore imitating a turbulent flow in nature identically with another turbulent flow is near impossible. The complexity and variation in scales with which the turbulent structures develop are mystifying to watch, and incredibly difficult to simulate or recreate. In laboratories, methods have been developed to create flows which are turbulent in nature through various techniques. Furthermore, with the advent of the computing age, simulations of turbulent flows have been created using computers and have been explored in the more recent past.

As with reproducing phenomena in a laboratory, there are always limitations to what can be done with computer simulations. As much as scientists and researchers would love to resolve flows down to the finest level, the computer limits the possible resolution achievable because of hardware and software limitations. There is a trade off between the largest scale of a system that is being examined, and the smallest possible resolution that the system can compute. There are many simulation techniques that have been developed to compute turbulence at any scale of resolution desired. Some are designed to reduce the complexity and computational cost. Possible simulation techniques range from direct numerical simulations (resolving all scales), to large eddy simulations, to Reynolds averaged Navier-Stokes simulations. Each approach or simulation method resolves details of the flow field and eddy motion to a certain extent, and then includes modeling terms for everything else it doesn't resolve.

The scope of this research lies in the direct numerical simulation (DNS) regime. DNS is direct simulation of fluid and it is governed by the full Navier-Stokes equations. In solving numerically the Navier-Stokes equations, this method directly resolves small

scale eddy characteristics and dissipation. It allows for full simulation of a flow field, with no modeling involved. This resolution carries a cost, and that is the immense computational time and computer memory required for carrying out these computations.

1.4 Initial Conditions

Simulations of decaying turbulence are dependent on the initial conditions used. Initial conditions to turbulent simulations are extremely important to the output of the simulation. There are many different approaches to the creation of initial conditions, covered briefly here.

As turbulence is seemingly random, the most basic and arguably most incorrect method for creation of a turbulent field is to assign random velocity values to points in space. The fundamental issue with this method is that it is not turbulence. It lacks the large scale structures that drive turbulence, and that contain most of the energy that ultimately passes down the energy cascade. When such a field is allowed to decay in time, it dies quickly due to the overwhelming viscous forces at small scales. The field is dominated by the small scale dissipation, and would be characteristic of the right side of the typical energy spectrum shown in figure 1-2.

A more technically sound approach to generating a turbulent initial condition is by forcing a pre-determined spectrum onto the velocity field. This would, by design, put the required amount of energy into the field that would then return an energy spectrum characteristic of a turbulent field. While this approach is more fundamentally sound, the flow field itself contains no large scale structures, just large scale energy. The lack of large scale structures in a physical field tends to not behave properly in the initial region of the energy cascade. In addition, the largest scale

behavior of the energy cascade is a topic of considerable debate. Simulations which set this behavior do not address this issue.

The approach used in this thesis is more physically realizable. It consists of the generation of a turbulent field by creating a situation in a flow field that develops into turbulence. In the experimental side of turbulent study, turbulence is typically created by passing flow through a grid. By having the flow move past a grid, there develops small turbulent wakes downstream of the grid. These small wakes merge, and energy is then transferred from the larger-scale grid size motions inherent in the flow to the smaller scales. The same method can be applied to the computational study of turbulence. By creating or modifying a flow in a computational domain, it is possible to create a physically realizable condition of turbulence. The methods used in this study are detailed in Chapter 2.

The initial conditions used for the two point correlation examination, as well as the Hallbäck strain study, were developed by Professor De Bruyn Kops.[2] They were initially developed from a spectral code for very large direct numerical simulations. Before becoming the initial conditions, the fields were progressed through time until a suitable fit to the energy spectrum was obtained. The resolution of the supplied fields was $768 \times 768 \times 1536$ grid points. These fields were averaged down to smaller resolutions for computations utilizing local machines in the lab because of computational limitations, as well as the amount of time required to perform small tasks with the exceedingly large fields.

1.5 Two-Point Correlations

Turbulence, in itself, is enigmatic. Comprised of multiple mixing length scales and eddies, quantifying such seemingly chaotic conditions is daunting. One of the earliest methods of quantifying turbulence is using two-point correlations. The concept of applying two-point correlations to turbulent flows was developed first by Taylor [3] and von Kármán [4]. Two-point correlations were the first method used to quantify the concept of the energy cascade, which is a fundamental concept in turbulent flows. The Fourier transform of the two-point correlation is closely related to the energy spectrum.

The basic concept of a two-point correlation is as follows. We let $\tilde{\mathbf{x}} = \mathbf{x} + \mathbf{r}$, where \mathbf{r} is the separation vector between the points \mathbf{x} and $\tilde{\mathbf{x}}$. The two-point correlation is defined as

$$R_{ij}(x, r) = \overline{u_i(x)u_j(\tilde{x})} \quad (1.1)$$

where $\overline{(\quad)}$ denotes an ensemble average, and Cartesian tensor notation is used for the indices. The correlation assigns a value describing how related the velocity at points $\tilde{\mathbf{x}}$ are to the velocity at point \mathbf{x} . The over bar indicates an ensemble average of many correlations. In terms of correlations, there are two classifications, the f- and g-correlations. The f-correlation is defined as the correlation of itself, with $f = R_{ii}(\bar{x}, \bar{x} + \Delta x_i)$. The g-correlation is defined as $g = R_{ii}(\bar{x}, \bar{x} + \Delta x_j)$. It is shown in Pope [1] that because of continuity, $\nabla \cdot \mathbf{u} = 0$, and assuming isotropy, the g and f correlations are related by equation (1.2).

$$g(r, t) = f(r, t) + \frac{1}{2} r \frac{\partial}{\partial r} f(r, t) \quad (1.2)$$

In this thesis, it is of interest to develop a method for predicting the two-point correlation that results when a wall is present. We are interested in the boundary conditions for R_{ij} . The equation for a two-point correlation at time $n+1$ is shown in equation (1.3), with the superscript $n+1$ denoting the time level.

$$R_{ij}^{n+1} = \overline{u_i^{n+1}(\mathbf{x})u_j^{n+1}(\mathbf{x}+\mathbf{r})} \quad (1.3)$$

It can be easily shown that the future velocity u_i^{n+1} at any point can be expressed as the known velocity u_i^n plus the change in velocity δu_i as it changes with time, or $u_i^{n+1} = u_i^n + \delta u_i$. In modifying equation (1.3) to reflect this, we can breakup both the future velocity, and the future shifted velocity, shown in the equations below, resulting in an expression for a two point expression at time $n+1$ based off of known quantities at time n , shown in equation (1.4).

$$R_{ij}^{n+1} = \overline{u_i^{n+1}(\mathbf{x})u_j^n(\mathbf{x}+\mathbf{r})} + \overline{u_i^{n+1}(\mathbf{x})\delta u_j(\mathbf{x}+\mathbf{r})}$$

$$R_{ij}^{n+1} = \overline{u_i^n(\mathbf{x})u_j^n(\mathbf{x}+\mathbf{r})} + \overline{\delta u_i(\mathbf{x})u_j^n(\mathbf{x}+\mathbf{r})} + \overline{u_i^n(\mathbf{x})\delta u_j(\mathbf{x}+\mathbf{r})} + \overline{\delta u_i(\mathbf{x})\delta u_j(\mathbf{x}+\mathbf{r})} \quad (1.4)$$

This equation can be further simplified by the fact that the first term, by definition, is the two point correlation at time n . Thus, the final expression for the correlation at time $n+1$ can be written as shown in equation (1.5).

$$R_{ij}^{n+1} = R_{ij}^n + \left[\overline{\delta u_i(\mathbf{x})u_j^n(\mathbf{x}+\mathbf{r})} + \overline{u_i^n(\mathbf{x})\delta u_j(\mathbf{x}+\mathbf{r})} \right] + \overline{\delta u_i(\mathbf{x})\delta u_j(\mathbf{x}+\mathbf{r})} \quad (1.5)$$

Equation (1.5) is comprised of the known terms R_{ij}^n , u_i^n , u_j^n , and the incremental changes in time of those respective velocity terms, denoted by δu_i and

δu_j . In the case of a wall suddenly appearing in a field of turbulence, the convective and diffusive terms of the Navier Stokes equations are negligible, and the pressure term dominates. In this case, we have $\delta u_i = -\frac{\partial(p\Delta t)}{\partial x_i} = -\frac{\partial\phi}{\partial t}$ shown more concisely in equation (1.6).

$$u_i^{n+1} = u_i^n + \delta u_i = u_i^n - \frac{\partial(p\Delta t)}{\partial x_i} \quad (1.6)$$

By making the above substitutions into the correlation equations, we arrive at equation (1.7), with the subscript s representing values at the shifted location.

$$R_{ij}^{n+1} = u_i^n u_j^n - \left[\overline{\frac{\partial p}{\partial x_i} u_{j_s}^n} + u_i^n \overline{\frac{\partial p}{\partial x_{j_s}}} \right] + \overline{\frac{\partial p}{\partial x_i} \frac{\partial p}{\partial x_{j_s}}} \quad (1.7)$$

From equation (1.7), it follows that the third term solely involving the pressure gradients of the field, can be split in half, and distributed among the first two terms. This is shown in equation (1.8), where the pressure terms are included with the velocity terms, that are bracketed in equation (1.7).

$$\begin{aligned} R_{ij}^{n+1} &= R_{ij}^n - \overline{\frac{\partial p}{\partial x_i} u_{j_s}^{n+1/2}} - \overline{u_i^{n+1/2} \frac{\partial p}{\partial x_{j_s}}} \\ &= R_{ij}^n - \left(\frac{\partial}{\partial x_i} - \frac{\partial}{\partial r_i} \right) \left(\overline{p u_{i_s}^{n+1/2}} \right) - \frac{\partial}{\partial r_i} \left(u_i^{n+1/2} p_s \right) \end{aligned} \quad (1.8)$$

We are interested in developing a model for the last two terms of this equation.

1.6 Application of Walls

The study of the effect of walls on turbulent flows has been studied extensively. However, most prior works are primarily concerned with the boundary layer effects and behavior. Boundary Layers have shear, which complicate the physics of the near wall

phenomena. This study aims to isolate the effect of the walls by removing the mean shear from the problem. Since it takes time for the viscous terms to begin to act, the early time behavior we are interested in is actually identical to the free-slip and no-slip boundary insertion problem. This study is concerned with the instantaneous insertion of a free slip non-permeable boundary to turbulence. That is, unlike a no-slip wall condition, fluid is allowed to move freely in directions parallel to the boundary. It is important to note that this makes no difference in this problem.

1.7 Low Reynolds Number Flows

Low Reynolds number flows are of particular interest to engineering applications. While most theory and modeling is done for high Reynolds number flows, Low Reynolds number flows include many important aspects that are not always present or of interest in high Reynolds number flows. Low Reynolds number flows include the near-wall region, and the free-stream region. Understanding low Reynolds numbers flows is of particular importance in many real world phenomena and processes, including internal combustion engines, and direct numerical simulations are one of the few ways to simulate the phenomena occurring in these flows. Of particular interest in this thesis is the case of flow undergoing axisymmetric strain.

The goal of this part of the work was originally to match work done by Dr. Magnus Hallbäck in his Doctoral thesis.[5] Hallbäck's extensive thesis covered many aspects of closure terms for the right hand side of the Navier Stokes. Of particular interest in this thesis is the work presented of Direct Numerical Simulation of axisymmetric contraction.

Axisymmetric turbulence is a simple turbulence situation that is not quite as fundamental as isotropic homogeneous turbulence. At moderate strain rates, this flow is difficult to model and makes an excellent test case. However, the initial conditions that led to the Hallbäck data are not well defined. Therefore, we wish to simulate this flow with precise knowledge of the initial conditions. He introduces a strain rate parameter, S^* defined in equation (1.9), as well as looking at the dependence on the turbulent Reynolds number, Re_T .

$$S^* = S \cdot \frac{2K}{\varepsilon} \quad (1.9)$$

The S in the above equations is defined as $S = \left(S_{ij} S_{ji} / 2 \right)^{1/2}$. The turbulent Reynolds number is defined as

$$Re_T = \frac{\nu K^2}{\varepsilon} \quad (1.10)$$

The strain rate tensor comes from the decomposition of the mean velocity gradient field in the Navier Stokes equations. The decomposition is

$$\frac{\partial U_i}{\partial x_j} = S_{ij} + \Omega_{ij} \quad (1.11)$$

The rate of strain tensor, S_{ij} , is given by equation (1.12). The last part of the decomposition, Ω_{ij} is the antisymmetric rate of rotation tensor, and is shown in equation (1.13).

$$S_{ij} = \frac{1}{2} \left(\frac{\partial U_i}{\partial x_j} + \frac{\partial U_j}{\partial x_i} \right) \quad (1.12)$$

$$\Omega_{ij} = \frac{1}{2} \left(\frac{\partial U_i}{\partial x_j} - \frac{\partial U_j}{\partial x_i} \right) \quad (1.13)$$

While Hallbäck investigated flows pertaining to axisymmetric contraction, expansion, and planar strain, the main focus his thesis pertains to axisymmetric contraction. A focus of his research was investigating the effect that varying levels of the strain rate parameter had on the anisotropy tensor a_{ij} . Using the definition of the mean gradient tensor, S , we can express equation (1.9) as

$$S^* = \sqrt{\frac{S_{ij}S_{ji}}{2} \frac{2K}{\varepsilon}} \quad (1.14)$$

Where S_{ij} is defined for axisymmetric cases as

$$S_{ij} = S \frac{2}{\sqrt{3}} \begin{pmatrix} 1 & 0 & 0 \\ 0 & -\frac{1}{2} & 0 \\ 0 & 0 & -\frac{1}{2} \end{pmatrix} \quad (1.15)$$

The comparison between Hallbäck's results and the modeling results of Jay Gadebusch is discussed in Chapter 3.

1.8 Decay Exponent

Understanding the decay of turbulence is an area of extensive research and study. It is relatively simple to create experiments that create decaying isotropic turbulence, and consequently easy to simulate with models of turbulence or even direct numerical simulations at lower Reynolds numbers. In the decay of turbulence, the large-scale momentum driven eddies drive the small scale dissipative eddies, where energy is taken out and converted to heat.

A characteristic of the decay of turbulence is that it is believed to have power law dependence in relation to its decay of turbulent kinetic energy. This power law behavior has become evident through many experiments and simulations.[1] As much

as it is agreed upon that there exists this power law decay of turbulence, there exists as much disagreement as to what the exponent should be. In the experiments by Comte-Bellot and Corrsin[6], they concluded the value of the decay exponent to be 1.26 for the kinetic energy. Other analysis was performed by Perot and de Bruyn Kops[7], highlighting the variety in the observed decay exponent. It is understood that the decay exponent has a strong Reynolds number dependence, with separate limits for both high and low Reynolds number decay. However, the exact Reynolds numbers dependence is still highly uncertain.

The focus of this report is the decay of low Reynolds number turbulence. Batchelor first proposed the value of the decay exponent for low Reynolds number decay of $5/2$. This value for the decay exponent is used in many models for the dissipation range of turbulence. However, as noted by Perot and de Bruyn Kops[7] and first pointed out by Saffman[8], the decay exponent even for low Reynolds number flow is dependent on how the three-dimensional energy spectrum behaves, in particular the low wavenumber portion of the energy spectrum. As described earlier, the low wavenumber portion of the energy cascade is representative of the energy contained in the largest scales. For the k^2 case, the decay exponent tends towards $3/2$ for low Reynolds number flow. However, for flows where the low wave number energy cascade behavior has a k^4 behavior, the decay exponent for low Reynolds number flow is the $5/2$ limit most commonly used by many models today.

The main issue with this discrepancy is that many models make use of the $5/2$ decay exponent; however the turbulent fields used are believed to have k^2 behavior in the low wave number regime. It should be said that the aforementioned $3/2$ and $5/2$

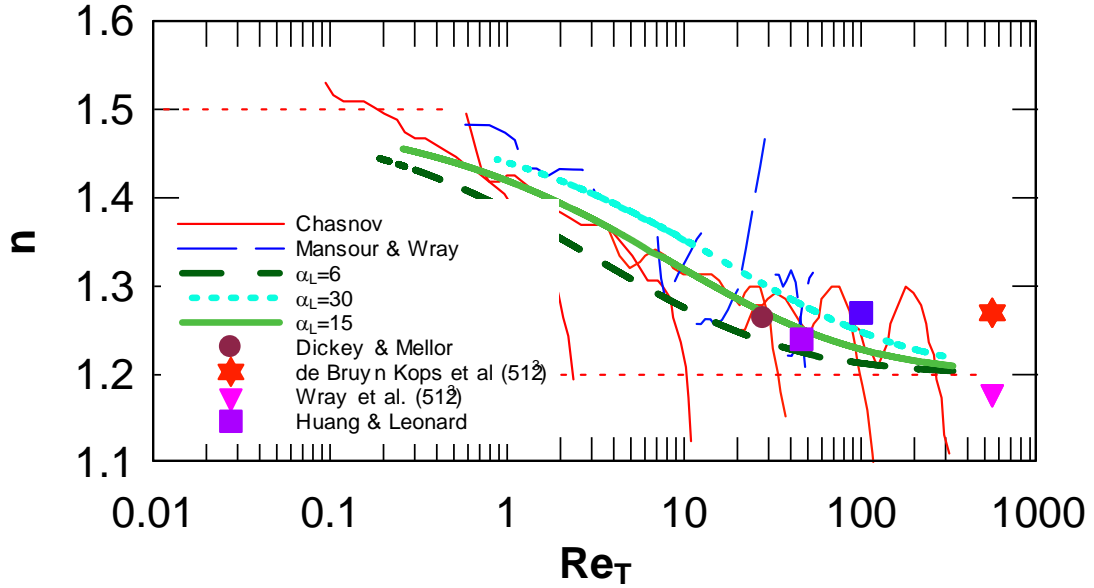


Figure 1 – 3: k^2 low wave number spectrum turbulent decay exponent, n , versus the corresponding turbulent Reynolds number, Re_T .

decay law exponents are the limits of the decay law exponent. Often, reported values for the decay exponent contain variety in their results. Figure 1-3 from Perot [7] illustrates the seemingly scattered reported values for the decay exponent, plotted against the turbulent Reynolds number, Re_T .

It is apparent that there is no definitive decay exponent value. The α_L values with their associated lines are generated from a model developed in from a k/λ model developed by Perot and de Bruyn Kops [7], in order to capture the transition behavior from high Reynolds number behavior to lower Reynolds number behavior.

In this study, the total kinetic energy is computed by equation (1.16), and the mass dependence is dropped for convenience,

$$K = \frac{1}{2} u_i^2 \quad (1.16)$$

Following equation (1.16), the expression for the kinetic energy decay and the dissipation can shown in equations (1.17) and (1.18). By combining those two

equations, the resulting expression for the power law decay for the dissipation is show in equation (1.19).

$$K = K_0 (t - t_0)^{-n} \quad (1.17)$$

Since

$$\frac{\partial K}{\partial t} = -\varepsilon \quad (1.18)$$

it follows that

$$\varepsilon = nK_0 (t - t_0)^{-n-1} \quad (1.19)$$

This implies that

$$T = \frac{K}{\varepsilon} = \frac{K_0 (t - t_0)^{-n}}{nK_0 (t - t_0)^{-n-1}} = \frac{1}{n} (t - t_0) \quad (1.20)$$

Therefore, the decay exponent can be expressed as the slope of the line representing how the turbulent timescale, $\frac{K}{\varepsilon}$, evolves in time.

CHAPTER 2

NUMERICAL METHODS

2.1 Overview

While there are many commercial computational fluid dynamics software packages available for use within the lab, it was advantageous to utilize an in-house code. Altering the boundary conditions and subroutine for solving the Navier-Stokes are significantly easier when one has access to the source code. The code has been used for developing turbulence (Gadebusch, [9]). It has also allowed for the same code structure to be expanded to include heat-transfer, forced turbulence generation (detailed in this thesis), and other turbulent flow studies, such as channel flow and drag reduction.

The method by which the code steps through time is a three step, second order Runge-Kutta method. Within each Runge-Kutta substep, matrix inversion is accomplished via the iterative conjugate gradient method. Incompressibility is enforced using the classical fractional step method. Essentially, at every time step there occurs a sequence of updating the new velocity and pressure at each point. The classical fractional step method is described extensively by Perot [10], and is only covered briefly in this thesis. A detailed explanation of how the conjugate gradient solver works is provided by Shewchuk [11].

The classic form of the Navier-Stokes equation, given by Wilcox[12], is

$$\rho \frac{D\mathbf{u}}{Dt} = -\nabla p + \rho \mathbf{f} + \nabla \cdot (2\mu[\mathbf{S}] + \zeta \nabla \cdot \mathbf{u}[\mathbf{I}]) \quad (2.1)$$

The use of bold letters indicates that the indices are applicable to all three directions. For example, the velocity \mathbf{u} , would translate into u , v , and w . The $\frac{D}{Dt}$ indicates the substantial derivative. The density of the fluid is represented by ρ , pressure by p , viscosity by μ , \mathbf{S} is the rate of strain tensor where $S = \frac{1}{2}(\nabla \mathbf{u} + \nabla \mathbf{u}^T)$, the second viscosity coefficient is ζ . In incompressible flow, $\nabla \cdot \mathbf{u} = 0$. Adding this to equation (2.1), Navier-Stokes is simplified to equation (2.2).

$$\rho \frac{D\mathbf{u}}{Dt} = -\nabla p + \rho \mathbf{f} + 2\mu \nabla \cdot [\mathbf{S}] \quad (2.2)$$

Although a long derivation, the divergence of the $\nabla \cdot [\mathbf{S}]$ term, which is the strain rate tensor, can be simplified to a simpler form, shown in equation (2.3).

$$\nabla \cdot [\mathbf{S}] = \frac{1}{2} \nabla^2 \mathbf{u} \quad (2.3)$$

Substituting equation (2.3) into equation (2.2), as well as making the assumption of constant density and viscosity, it yields a simpler form of Navier-Stokes, shown in equation (2.4).

$$\frac{Du}{Dt} = -\nabla \left(\frac{p}{\rho} \right) + \mu \mathbf{f} + \nu \nabla^2 \mathbf{u} \quad (2.4)$$

The above form of the Navier-Stokes can be viewed symbolically as having a convective term, a diffusive term, and a pressure term, shown in equation (2.5).

$$u_i^{n+1} = u_i^n + (C_i + D_i + P_i) \Delta t \quad (2.5)$$

Equation (2.5) represents the Euler explicit advancement. Using the fractional step method, the code solves for the updated velocity field by breaking up equation (2.5) and solving for the convective and diffusive portions first, and then adding the pressure term to the incremental $\hat{\mathbf{u}}_i^{n+1}$, shown in equation (2.6), and outlined in [10].

$$\begin{aligned}\hat{\mathbf{u}}_i^{n+1} &= \mathbf{u}_i^n + \left[C_i(\mathbf{u}_i^n) + D_i(\mathbf{u}_i^n, \mathbf{u}_i^{n+1}) - \nabla p_i^n \right] \Delta t \\ \mathbf{u}_i^{n+1} &= \hat{\mathbf{u}}_i^{n+1} - \nabla(p_i^{n+1} - p_i^n) \Delta t\end{aligned}\tag{2.6}$$

From equation (2.6), it can be shown that

$$\nabla^2(p_i^{n+1} - p_i^n) \Delta t = \nabla \cdot \hat{\mathbf{u}}_i^{n+1}\tag{2.7}$$

since by incompressibility it follows $\nabla \cdot \mathbf{u}_i^{n+1} = 0$.

As mentioned above, the code utilizes a Runge-Kutta time marching method (RK3) that is second-order accurate. While more information on the technique can be found in Anderson[13], a brief review of the algorithm is reviewed in equation (2.8).

$$\begin{aligned}\tilde{y}_{n+\frac{1}{2}} &= y_n + \left(\frac{1}{2} \Delta t\right) \cdot f(y_n) \\ \tilde{\tilde{y}}_{n+1} &= y_n + (\Delta t) \cdot f(\tilde{y}_{n+\frac{1}{2}}) \\ y_{n+1} &= \tilde{y}_{n+\frac{1}{2}} + \left(\frac{1}{2} \Delta t\right) \cdot f(\tilde{\tilde{y}}_{n+1})\end{aligned}\tag{2.8}$$

In equation (2.8), the terms \tilde{y} and $\tilde{\tilde{y}}$ represent intermediate solutions containing both velocity and pressure information, arrived at via equations (2.6) and (2.7). This low storage method of time marching is particularly useful when performing large resolution simulations.

In order to perform high resolution direct numerical simulations, it is necessary to parallelize the code. In parallel computing, a few additional subroutines and modules are needed in order to support the communication of information between each

subdomain located on different nodes of a supercomputer. These libraries and custom subroutines are extensively covered in Gadebusch. [9]

2.2 Meshing

The code makes use of a staggered Cartesian mesh, explained in this section. A three-dimensional Cartesian mesh means that each cell of the mesh is a cuboid. This implies that the opposing faces of the cuboid are parallel, and aligned with the global coordinate system. This uniformity allows for many averages, gradients, Laplacians, and other operations on the velocity and pressure fields to be computed efficiently. It also allows for simple cell indexing.

Describing the mesh as staggered refers to the way information within each cell is stored. In collocated methods, all information regarding a particular cell, such as the velocity vector and pressure, is stored in the center of the cell. In a staggered mesh, each component of the velocity is stored on the cell faces, and the pressure pertaining to that cell is stored at the center. A sample cell of this type of storage is shown in figure 2-1.

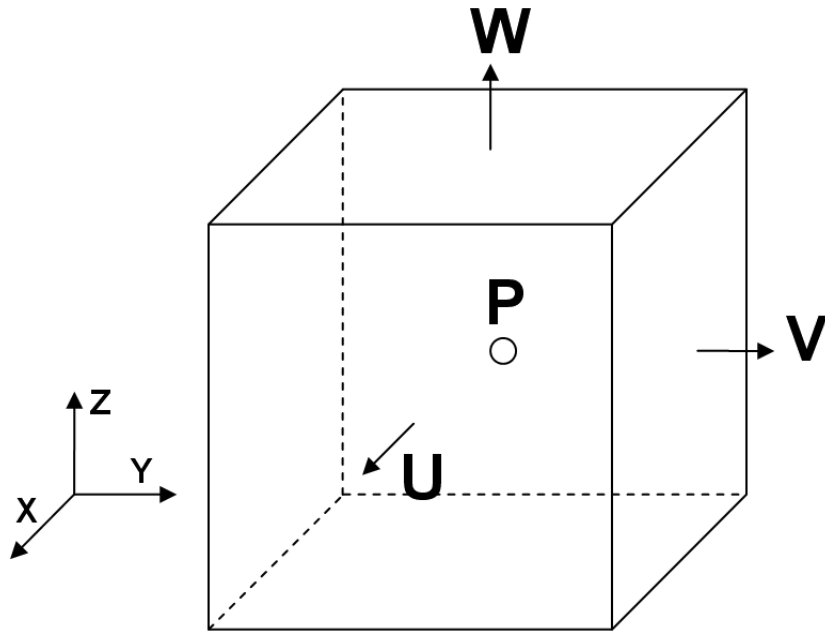


Figure 2 – 1: Example of velocity distribution and pressure distribution about each cell in the staggered mesh.

As detailed in figure 2-1, each component of the velocity is stored on its respective face. The x-component of the velocity, **U**, is stored at the face of the cell normal to the x-axis. Similarly, the y-component of the velocity, **V**, and the z-component, **W**, are stored at their respective normal faces. The pressure associated at each cell, **P**, is stored centric to the cell. This is advantageous when working with the presence of walls, as is done in this thesis. It allows velocities to be set exactly where the wall would be in the field of turbulence, and avoid pressure singularities that would arise with the instantaneous insertion of a wall. Staggered mesh methods also have unique conservation properties, such as mass, momentum, kinetic energy, and vorticity. They also have no artificial dissipation.

The overall domain used for much of this thesis is cuboid in nature. If we denote n as a characteristic length, the length of each side of the domain used for this study in the (x, y, z) coordinates would be $n \times n \times 2n$. The initial conditions supplied by Professor De Bruyn Kops [2] had a domain size of $18\pi \times 18\pi \times 36\pi$.

2.3 Two-Point Correlations

Starting from the basic code, subroutines were added to compute two-point correlations of the velocity fields. Starting from the basic two-point correlation definition given in equation (1.1), correlations were created based on the staggered mesh velocity fields produced by the code.

The correlations, generally shown graphically along a line, are constructed in three-dimensions within the code. To begin, the code allocates a correlation field, referred to as the correlation space, in which the three-dimensional two-point correlation will be assembled. Each point in the correlation space essentially represents the distance from the center of the correlation, i.e. the center point $(0,0,0)$ would indicate the velocity field correlated at a separation of $\vec{r} = (0,0,0)$. For every point in the correlation space, an array of shifted locations is built, based on the point's distance to the center of the correlation space. These shifted points are indicated by hats, as shown in equation (2.9).

$$\hat{\mathbf{u}}_i = \mathbf{u}_i(x + r_x, y + r_y, z + r_z) \quad (2.9)$$

A summation is then taken of each point in the velocity field correlated with its associated shifted point. It is important to note here that for correlations taken involving the wall, the summations were only planar, parallel to the wall. For isotropic

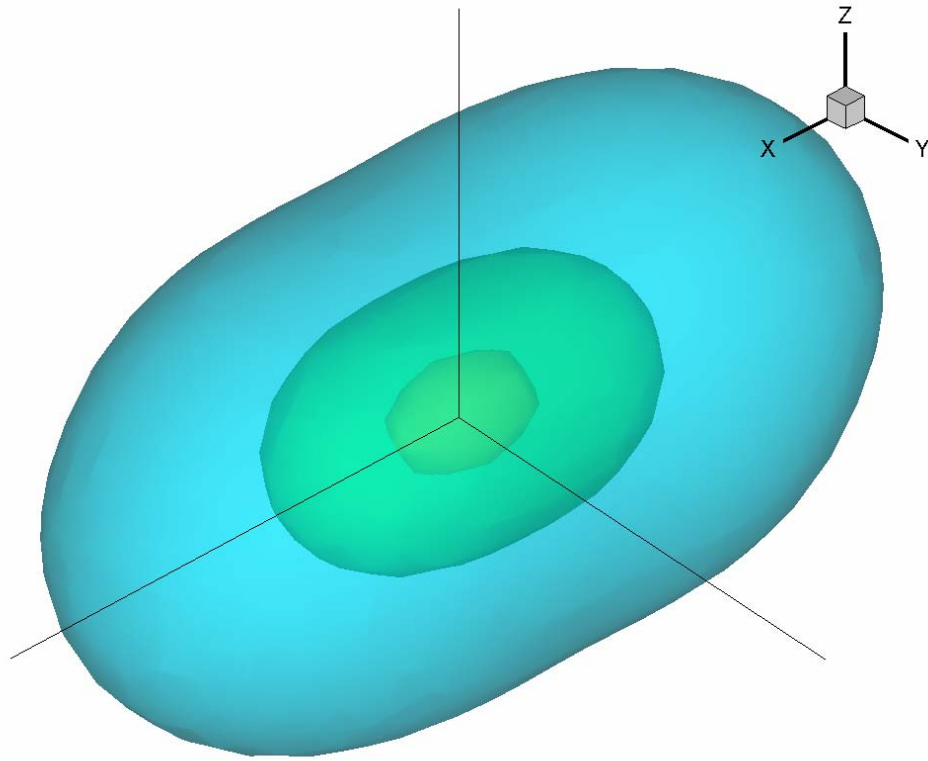


Figure 2 – 2: A three-dimensional view of a R_{11} correlation using transparent iso-surfaces to show intensity values.

cases, the summations are taken in all three directions. The summation is detailed in equation (2.10)

$$R_{ij} = \overline{\mathbf{u}_i \hat{\mathbf{u}}_j} \quad (2.10)$$

The over bar in equation (2.10) formally represents ensemble averaging, but in practice is a spatial average over homogeneous directions. Because we are interested in the behavior of the correlations near the wall, the averaging does not take place over the entire domain. With the wall located on the y -faces of the domain, averaging is only performed in the homogeneous x -, and z -direction, and consequently not in the inhomogeneous y -direction. The resulting correlation space field created by the two

R22 F Correlation

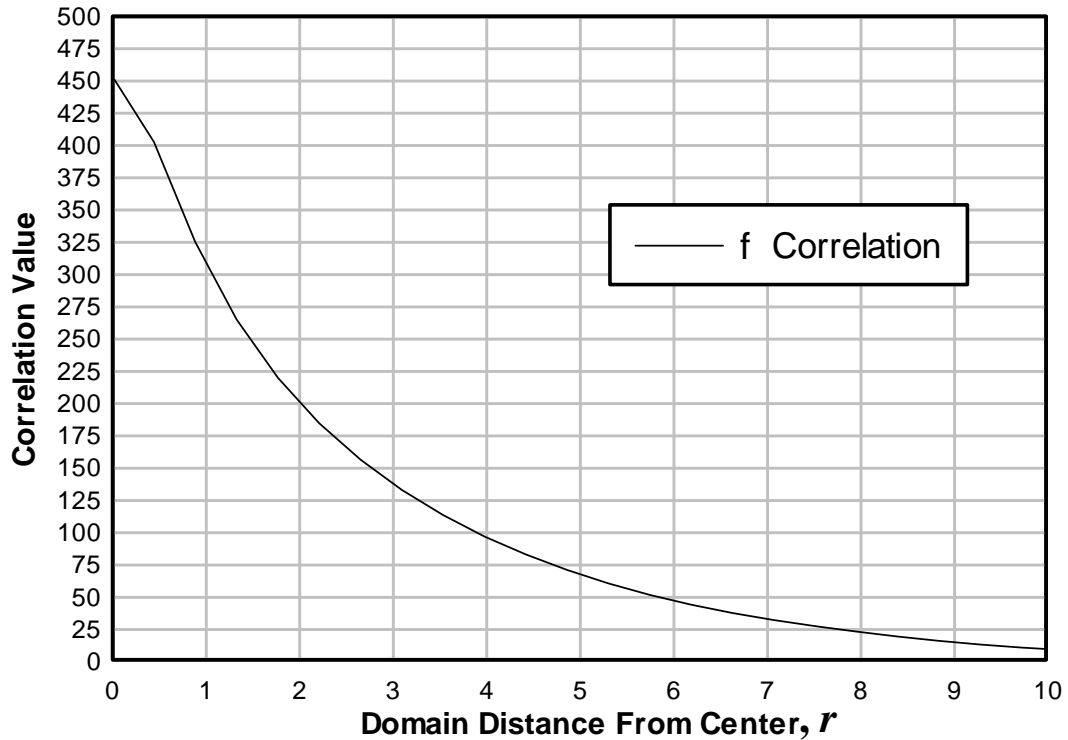


Figure 2 – 3: A typical f-correlation of isotropic homogenous turbulence, in this case the R_{22} f-correlation (from 32^3 field).

point correlations in the velocity fields is a three dimensional correlation. An example of the three dimensional field is shown in figure 2-2. In order to generate a standard visualization of the correlation versus distance from the center, it is necessary to look at the values along a line extending from the center of the correlation. A typical f-correlation is shown in figure 2-3, and is created simply by examining the values extending outwards along the center axis in the corresponding velocity direction (x -direction for R_{11} , y -direction for R_{22}).

Figure 2-2 utilizes iso-surfaces to demonstrate the shape of the correlation in three dimensions. It has a characteristic ellipsoidal shape that is elongated in the velocity

direction. It is casually referred to as a “submarine” shape, as one would imagine what the main portion of a modern thermonuclear submarine looks like.

When looking at the constitutive parts of the correlation given in equation (1.5), the same process of creating the correlation fields documented above are used. However, consideration of what velocity and pressure differences that are being combined becomes important. The staggered mesh, while useful for many aspects of numerically solving the discretized Navier Stokes, necessitates careful accounting of the locations of the pressures and velocities in the cell when taking derivatives and differences in regards to the two point correlations. An example of would be performing correlations involving both the pressure and the velocity. The pressure is stored at the center of the cell, while the velocity in the cell is stored at the faces. In order to take a $\overline{pu_i}$ correlation at the point (32,32,32), for example, simply taking the product of the pressure and velocity at (32,32,32) would not yield the $r=0$ correlation value. In order to adequately perform such a correlation, either the velocity at the center of the cell, or the pressure at the face, needs determining.

2.4 Greens Method

In order to verify that the conjugate gradient solver behaves correctly with the addition of the boundary conditions the wall imposes, an alternative solution approach, a Greens method approach, was also developed to predict the velocities near the wall. The method is useful in solving differential equations that have simple boundary equations.

The motivation behind applying Greens method to solve for the flow was to verify that the conjugate gradient solver was behaving properly in predicting the velocity field with the insertion of the wall. We start with an expression for the divergence of the velocity, shown in equation (2.11). This is non-zero only in the cells next to the wall. For a general image of how the Greens method is applied in the code, a graphical representation is shown in figure 2-4.

$$\nabla \cdot \mathbf{v} = \frac{v_{wall} A_{wall}}{V} = \frac{v_{wall}}{\Delta y} \quad (2.11)$$

In the figure, taking the divergence of the velocity next to the wall, it can be shown from equation (1.6) that taking the divergence of both sides yields the equality shown in equation (2.12).

$$\begin{aligned} u^{n+1} &= u^n - \nabla(p\Delta t) \\ \nabla \cdot u^{n+1} &= 0 = (\nabla \cdot u^n) - \nabla^2(p\Delta t) \\ \nabla^2(p\Delta t) &= (\nabla \cdot u^n) \end{aligned} \quad (2.12)$$

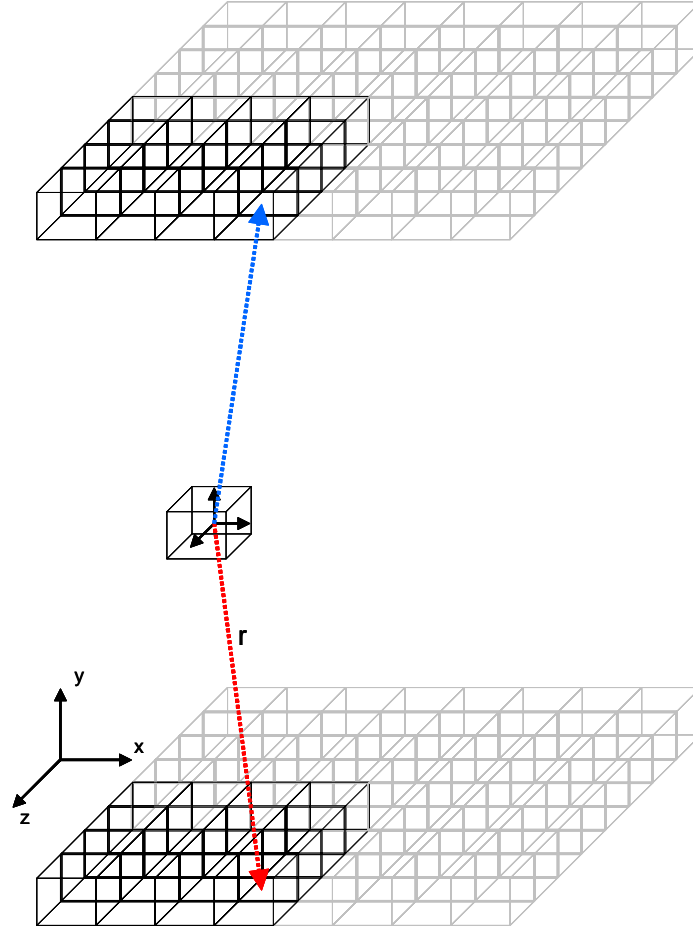


Figure 2 – 4: Representation of how the code develops and calculates the Green method approach.

It is important to note that equation (2.12) is the reduced Navier-Stokes equations for wall insertion. The last line of equation (2.12) is also solved by the conjugate gradient solver. Our approach to solving this resulting Poisson equation is the Greens function solution. The source term ϕ is defined as $\phi = (p\Delta t)$, and the equation needing solving is $\nabla^2\phi = S$. The solution to this is shown below in equation (2.13). S is the source from the cell, and r is the distance from the cell to the location ϕ .

$$\phi = \iiint S \cdot \frac{1}{4\pi r} d\bar{x}' = \iiint \frac{S(\bar{x}')}{4\pi|x-x'|} d\bar{x}' \quad (2.13)$$

Since $S(\vec{x}')=0$ everywhere but the line of cells next to the wall, the triple summation can be reduced to a summation over the cells adjacent to the wall. Following the above, the pressure term in the right hand side of equation (2.12) can be expressed as shown in equation (2.14).

$$(p\Delta t)^{(x)} = \left[\sum_{x'} \sum_{z'} \frac{v_{wall}(x', 0, z')}{\Delta y} \cdot \frac{1}{|x' - x|} + \sum_{x'} \sum_{z'} \frac{v_{wall}(x', 0, z')}{\Delta y} \cdot \frac{1}{\begin{bmatrix} x' - x + \\ -\Delta y \\ 0 \end{bmatrix}} \right] \quad (2.14)$$

This equation is summed over both x' and z' . The prime notation denotes locations along the wall. The last term in equation (2.14) represents the reflection term, a concept discussed extensively later in this thesis.

2.5 Initial Condition Generation

Rather than initializing turbulence as a sequence of random numbers, we wish to generate it in a manner that is closer to reality, or physically realizable. The generation begins with an initial condition of zero velocities and pressure field. From there, the field is progressed through time, with different modifications made to the solution of the Navier-Stokes equations and boundary equations within the domain to simulate physical conditions that mimic actual turbulence creation.

The incompressible Navier-Stokes solved by the code is given in equation (2.15).

$$\frac{DU}{Dt} = -\frac{1}{\rho} \nabla p + \nu \nabla^2 U \quad (2.15)$$

The density term, ρ , is omitted for convenience, as it could be assumed that $\rho = 1$. By inspection, the right-hand side of the Navier-Stokes equation is comprised of acceleration based terms. The first approach to generating turbulent fields was insertion of jets into the domain. The method developed was to add an acceleration term, a_{jets} to the Navier-Stokes equation,

$$\frac{DU}{Dt} = -\frac{1}{\rho} \nabla p + \nu \nabla^2 U + a_{jets} \quad (2.16)$$

In this arrangement, an array of jet accelerations was created such that $a_{jets} = 0$ in most locations, and $a_{jets} \neq 0$ in only a few locations. In order to not arrive at a steady state condition after some time, it was determined that the jets would be required to be changing in direction, location, and magnitude as a function of time. Therefore, each jet would operate on propelling the fluid at a location for a fixed amount of time, and then stop. The timescale generally associated with turbulent flows is given as τ ,

where $\tau = \frac{K}{\varepsilon}$.

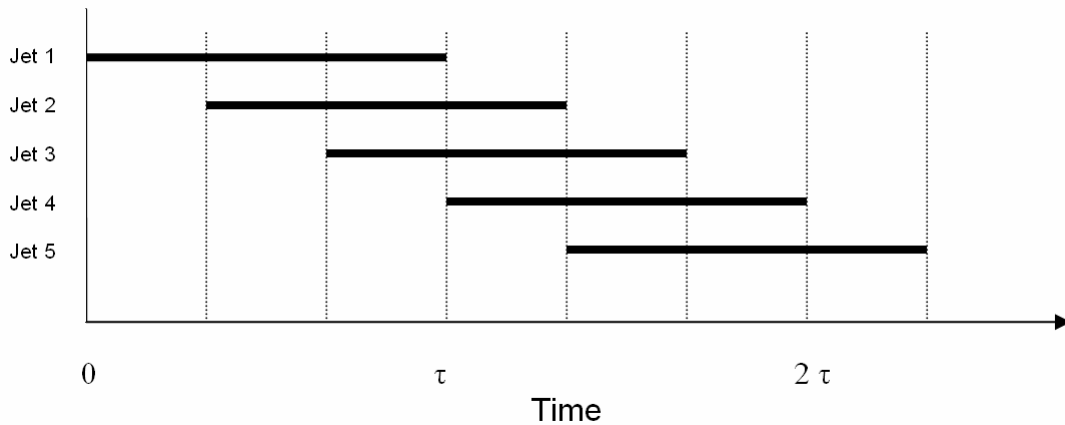


Figure 2 – 5: A pictorial representation of the jet activation concept.

K is the total kinetic energy in the system, and ε is the rate of dissipation in the field. This timescale was the basis for how long each individual jets should remain on. The timescale τ was divided by the total number of jets, which yields the increment of time between each deactivation of a jet reaching the end of its τ duration, and the activation of a new jet to being. This can be visualized by figure 2 – 5. The magnitude of each jet was constant, but each new jet position and its orientation were picked randomly. The method of establishing random numbers was to make use of the intrinsic random number generator subroutine built into Compaq Visual Fortran Standard Edition 6.6.0 as a f90 function. It uses the command `Random_seed()` to seed where in the random number sequence it begins, based off of the current date and time. It then has a command to fill a single variable or an array with random numbers, each number between 0 and 1. A more detailed look at the methodology behind the random number generator is shown in the Compaq Visual Fortran Standard Edition 6.6.0 help files, with details the functionality of the generator, and references the studies published about the algorithm it uses.[14, 15]

As stated before, the field is initialized with a zero velocity condition. A full jet array is initialized, with randomly located and oriented jets. The code then progresses through time, with the fluid accelerating at the jet locations, and turns off the appropriate jets after they have run for one turbulent timescale, while activating a new randomly located and oriented jet. The one caveat in this randomness associated with assigning random jet locations and orientations is that without monitoring, jets can be placed directly next to each other, causing divergence issues at random times. Therefore, a subroutine was created to ensure that jet locations would not be chosen if they were within a certain distance of any existing jet. If a random location fell within this tolerance of any existing jet, it would be discarded, and a new random location chosen.

A second approach utilized for generation of turbulent initial condition is the presence of cubes in a flow field. Inspired from how grid turbulence is created (flow through a series of grids), flow is passed through an array of randomly distributed cubes in a domain area. The cubes themselves have a user determined size. The same method of checking jet locations was applied to the randomly chosen box locations, in order to prevent boxes from overlapping each other. Overlapping boxes will cause divergence issues because of the application of the box boundary conditions, which involves specifying velocity conditions and pressure gradients. The flow is driven past the cubes by a uniform pressure gradient that is randomly oriented and which changes once a turbulent timescale has elapsed.

CHAPTER 3

RESULTS

This chapter is divided into seven separate sections, (1) wall insertion, (2) the validation of the Green's Method, (3) two-point correlation results, (4) vorticity, (5) low Reynolds number strain flow, (6) the generation of new initial conditions, and (7) decay law studies.

3.1 Wall Insertion

This research concerns the effect of instantaneous wall insertion into homogeneous isotropic turbulence. In order to simulate the presence of a wall in the domain, both the velocity fields and the pressure field needs to be modified. The wall being inserted into this simulation is a slip wall. The slip wall specifies a zero penetration boundary condition at the wall, but fluid parallel to the wall is free to move. Furthermore, the slip wall specifies that the normal velocity gradient of the tangential velocities ($\frac{du}{dy}$ and $\frac{dv}{dy}$ in this study) at the wall to be zero. An example wall is shown in Figure 3.1. The shaded faces are representative of the faces of the domain with the wall boundary conditions imposed. The slip wall is the appropriate choice of a wall boundary condition for this study, because viscous effects take time to affect the flow, and the pressure effects (such as wall insertion) are instantaneous. There is no difference between a slip or no-slip wall at the early times of interest in this work.

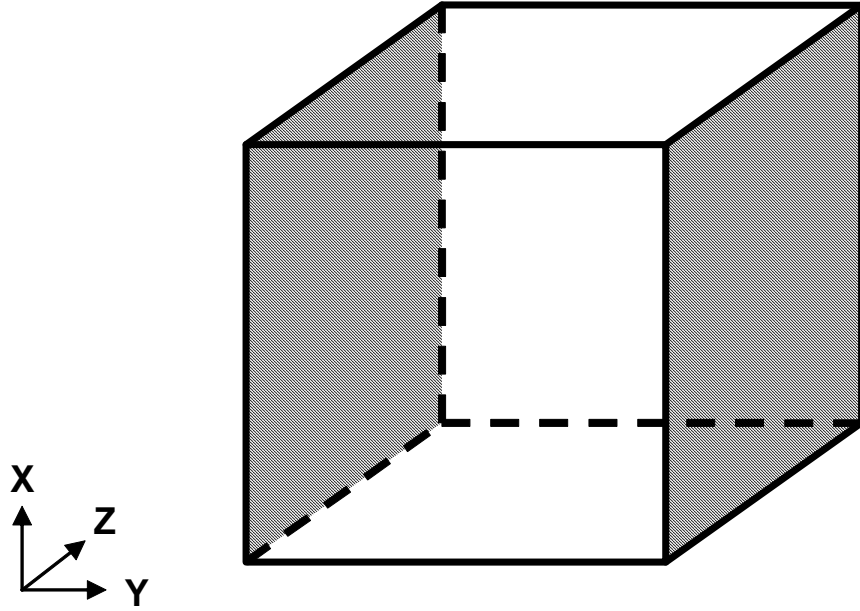


Figure 3 – 1: Simulation domain showing where the boundary conditions are imposed (shaded sides).

Much of the work on the insertion of walls was performed with the walls on the X-Z faces at the end of the domain. Other wall arrangements were investigated. The purpose of investigating the field with the walls placed in other orientations was to gain a greater statistical sample base for the results. Isotropic Turbulence is characterized by its statistics being independent of directionality. While the results shown later in this chapter indicate some directionality (discussion in Section 3.2), the initial fields are considered isotropic, and in the regime of the center of the correlations, the effect of the skewness becomes insignificant. The boundary conditions at the wall are

$$\left. \frac{du}{dy} \right|_{wall} = \left. \frac{dw}{dy} \right|_{wall} = 0, \quad v|_{wall} = 0 \quad (3.1)$$

The insertion of the wall carries implications for the pressure field. A characteristic of the rapid insertion of walls into a flow is that the pressure undergoes large fluctuations in order to correct for the sudden imposition of the perpendicular velocity boundary condition of $v=0$. The boundary condition at the wall for the pressure is that the derivative with respect to the wall normal direction is zero as shown in equation (3.2).

$$\left. \frac{dp}{dy} \right|_{wall} = 0 \quad (3.2)$$

In this work, only one time step is performed, as that is the problem of interest. These boundary conditions were applied explicitly in the solver subroutine of the code. Because of the very small timestep, the viscous terms are negligible and the tangential velocity boundary conditions, equation (3.1), are irrelevant

3.2 Green's Method Validation

In order to check the results from the Navier-Stokes code being used, it was determined to apply a Green's function method to determine the same solution and confirm the same values for the near wall velocities as the Navier-Stokes solver produces. After successful implementation of the algorithm explained in section 2.3, the results of the pressure field after the wall was inserted were found to agree well.

Figure 3-2 shows an output of the two different methods. Each image in Figure 3-2 is a XZ planar slice of the pressure at a grid location of $j=1$ just after the wall has been inserted. This represents a slice of the flow that is parallel to and very close to the wall being inserted. This figure shows the contours of the pressure at one grid point away from the wall. The image on the right is from the Navier-Stokes code and the

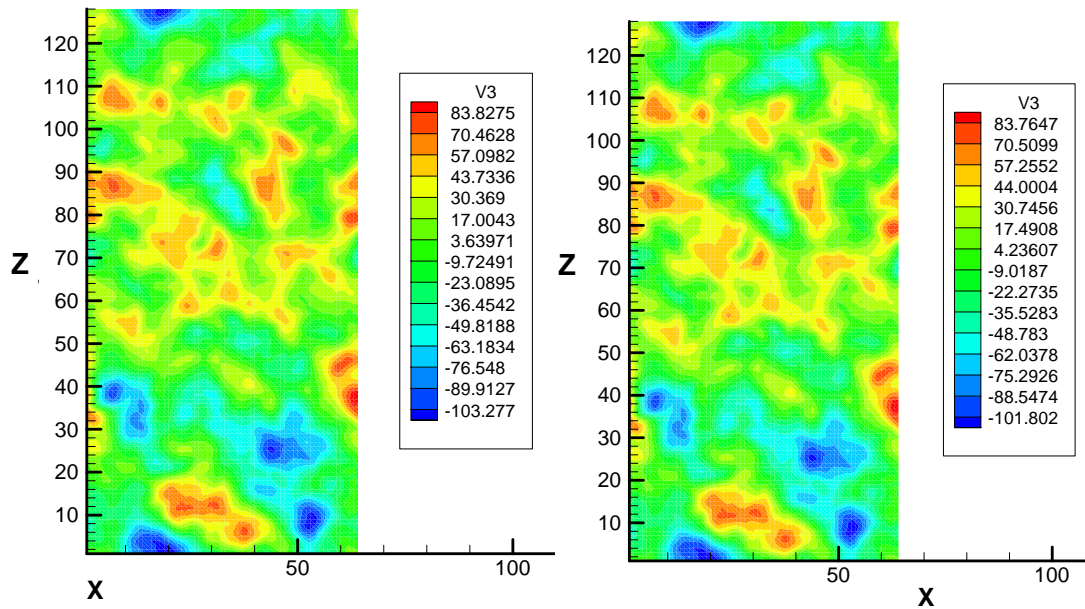


Figure 3 – 2: Comparison of pressure fields. The left field is generated from the Greens method, and the right field is generated from the Navier-Stokes solver.

image on the left is the solution from using the Green’s function method. The contour levels shown in the legends show that the two methods generate extremely similar results for the pressure field. It is not expected that they be exactly the same, because the accuracy of the Greens method is directly related to the extent of the summation terms which in theory should go to infinite distance.

In performing the Green’s function method for computing the velocity and pressure fields after the wall is inserted, we observed a large disparity in the computational time required to complete the calculations. In a relative sense, the Navier-Stokes method completed in about a tenth of the time that the Green’s function method required. The cause of the longer time to calculate the result with the Green’s function method is due to the double summation that it requires. In order for it to be accurate, it needs to perform many summations over the wall plane area. In order to

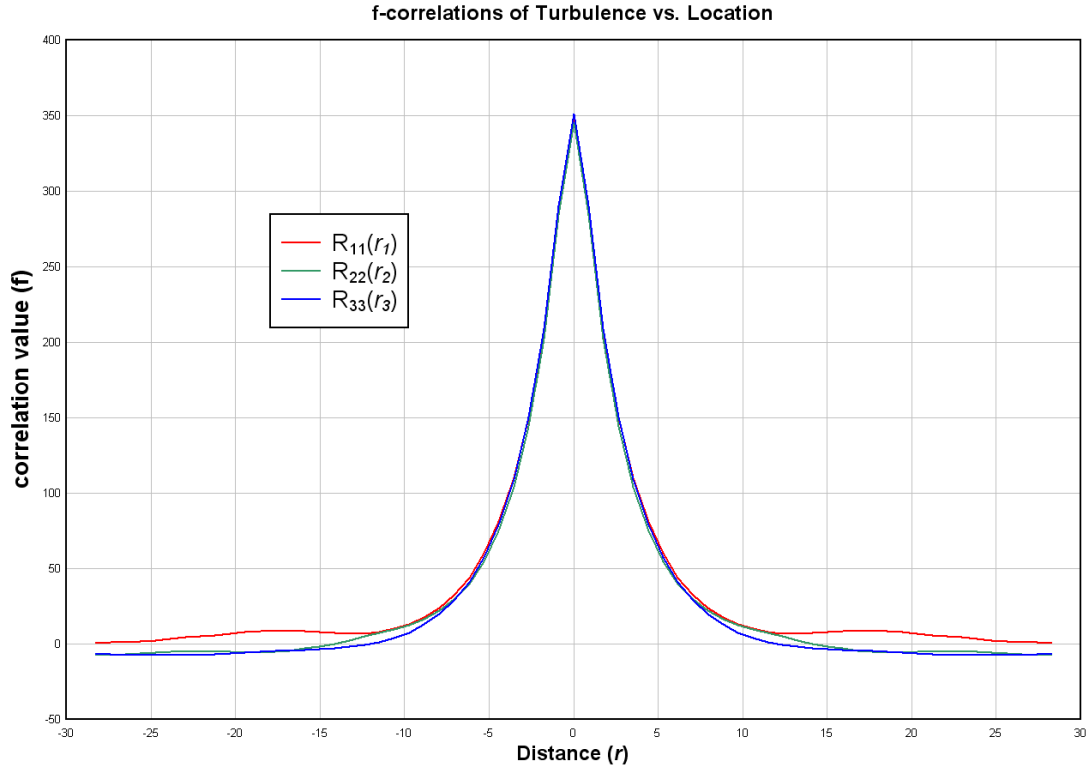


Figure 3 – 3: f-correlations of the initial velocity fields before the wall is introduced. $Re_T = 640$.

become reasonably close, the wall plane is extended via periodicity, and the summations are performed over three to four wall lengths.

3.3 Two-Point Correlations

The main method used in this thesis for analyzing the velocity fields and how they react to the sudden imposition of a wall is two-point correlations of the velocity fields. Figure 3-3 is the f-correlation of isotropic at a turbulent Reynolds number of $Re_T = 640$. As discussed previously, the two-point correlations are a function of the separation distance which is three dimensional. The common presentation of the correlations in this thesis will be two dimensional slices of this three dimensional structure, shown previously in figure 2-2. There are also comparisons performed in one

dimension, which are useful for understanding the proposed model for predicting how walls influence the turbulence statistics.

The two-point correlation performed on the initial conditions return a profile typical for isotropic turbulence. This data is from a $256 \times 256 \times 512$ DNS simulation, but only every 8th data point is used in the data post-processing. This makes the results for $r \geq 3$ inaccurate, but the resulting shape for larger r is unaffected. The domain size for the field is 18π , so the extents of the correlations in figure 3-3 represent half the domain size. For the classical f-correlation the scale is normalized by the peak value at the center.

The correlations shown in Figure 3-3 are f-correlations. There is debate about whether the f-correlation should become negative at large separation distances. After verifying the technique in the code, it was shown these negative tails do exist for this flow field, but they decrease to zero as $r \rightarrow \infty$.

The next step in analyzing the two-point correlations was gaining an understanding of the two-dimensional representations of the correlations. The correlation space is shown in two dimensions in figure 3-4.

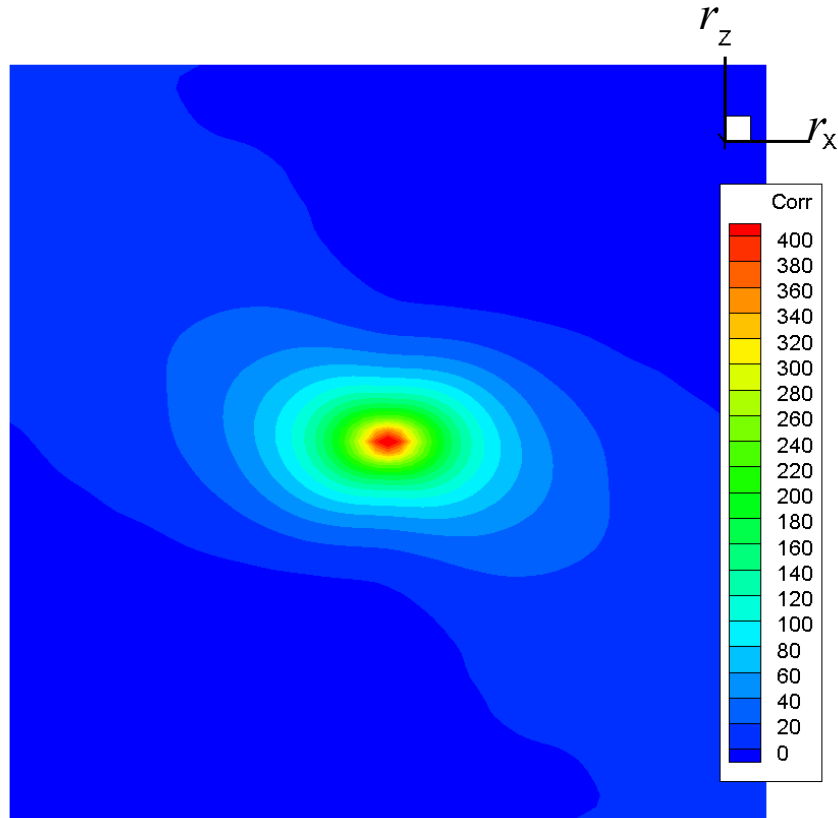


Figure 3 – 4: R_{11} correlation looking at the r_x - r_z Plane at $r_y = 0$.

The two-dimensional field in figure 3-4 shows the highest area of correlation in the center of the field, and it tapers off as the distance from the center increases. This image is a R_{11} correlation, which is the correlation of the v-velocities at two different points separated by distance r . It is a X - Z planar slice of the correlation field where $r_y = 0$. It is an averaged correlation, (over x , y and z) before the wall is introduced. Following the discussion of two-point correlations from previous chapters, the f-correlation could be constructed by picking the values along the x -axis where $r_z = 0$. The two-dimensional correlation field also contains the g-correlation as well. This

correlation could be constructed by extracting the correlation values along the r_z -axis where $r_x = 0$.

The image presented in figure 3-4 demonstrates an important issue that was of concern throughout this thesis. The R_{11} correlation above has what is referred to as “skewness” in it. This means that the correlation is not symmetric about the two axes. In isotropic homogeneous turbulence, there should be symmetry about every axis. This figure suggests that the velocity fields in the initial conditions are not truly isotropic for the large scale eddies. It is still not entirely clear if this defect is mostly cosmetic or if it leads to an alteration of the results for the wall insertion problem.

Other initial conditions generated by Professor de Bruyn Kops[2] were investigated using two-point correlations. Inherent skewness was also present in those fields. While it was determined that the initial conditions being used for the two point correlation study were skewed, the important region near the center of the correlation was still characteristic of isotropic turbulence, and the skewness only had an effect on the largest r values of the correlation space. Figure 3-5 shows an r_x - r_z slice through the center ($r_y = 0$) of the R_{11} correlation space and a closer view of the center of the correlation space on the same plane. The axis r_x and r_z refer to the separation distance. This figure is similar to figure 3-4, and is included to the comparison of the skewness present in the greater r values, and the absence of the skewness in the lower r values, shown in the zoomed-in view on the right.

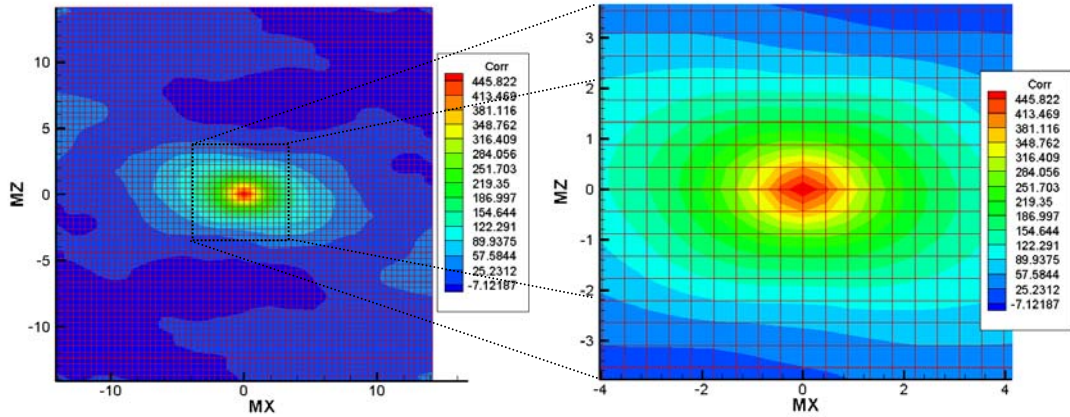


Figure 3 – 5: r_x-r_z planar slice of R_{11} correlation at $r_y = 0$ (left), Center of R_{11} correlation zoomed in (right).

While these initial conditions were used in this research, it is shown in latter sections of this chapter that the inherent skew present in the initial conditions do have an effect on the strain flow study. For the purposes of the wall insertion investigation, they were deemed suitable for use.

Using the Navier-Stokes method and the initial conditions detailed above, the wall was inserted. For the purposes of this research, the main correlation of interest is the R_{22} correlation, and its diagonal constituents, the R_{21} , R_{23} , R_{32} , and R_{12} correlations. The correlation tensor is not symmetric after the wall insertion. While equally interesting, we have found that the other components of the correlation tensor (R_{11} , R_{13} , R_{31} , and R_{33}) are not as profoundly affected by the wall insertion and are much harder model.

The R_{22} correlation of isotropic turbulence is shown in figure 3-6. This is a r_x-r_y slice of the three-dimensional correlation field at $r_z = 0$. Similar to the R_{11}

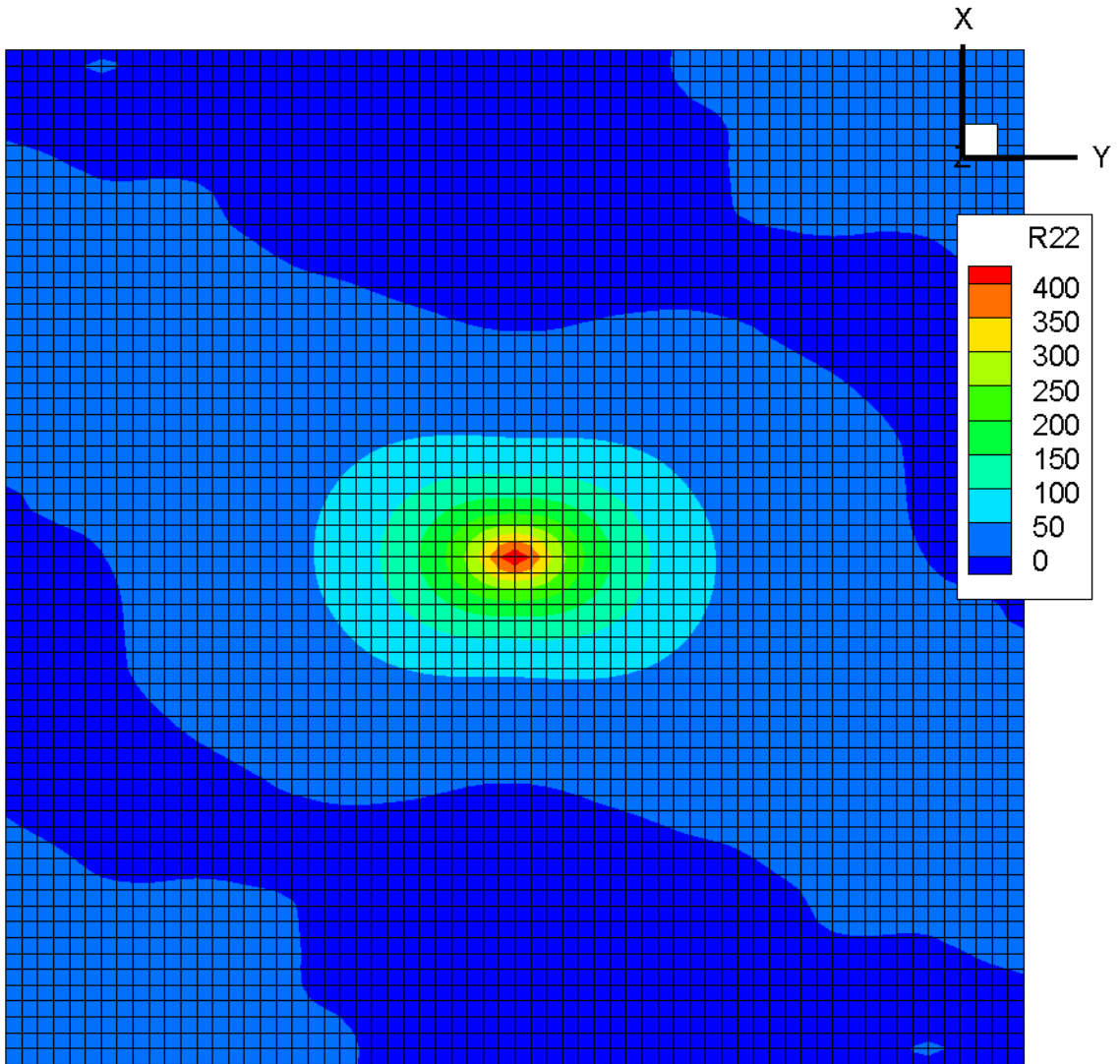


Figure 3 – 6: A r_x - r_y planar slice of the R_{22} correlation field through $r_z = 0$.

correlation, the R_{22} correlation is characteristically longer in the r_y -direction representing the f-correlation, and the g-correlation can be viewed as the correlation values extend in the r_x direction.

Figure 3-6 is the initial R_{22} correlation before the wall insertion. It is shown as a basis for comparison to the correlation after the wall was inserted, which is shown in figure 3-7. As with the pre-wall condition shown in figure 3-6, the post-wall condition

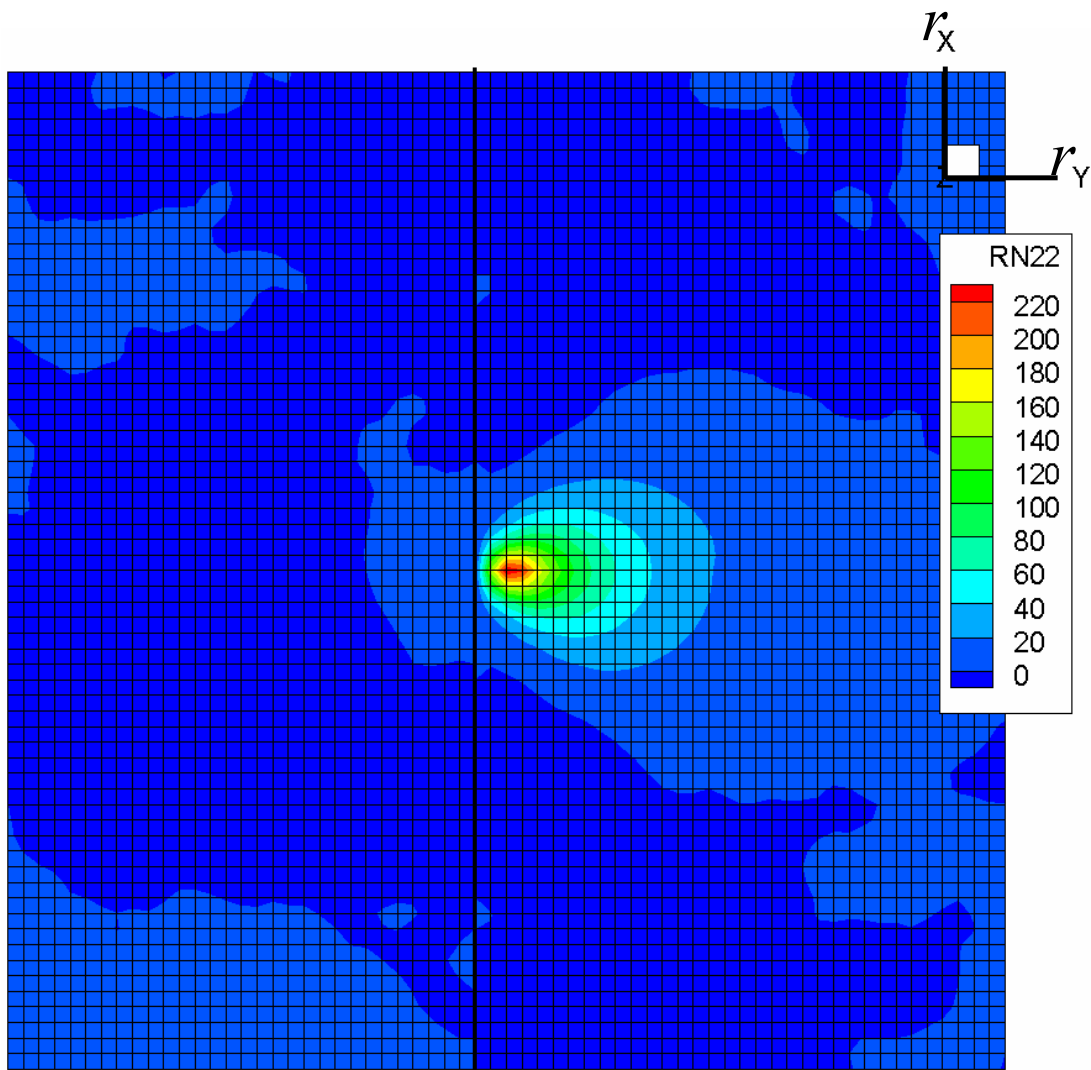


Figure 3 – 7: A r_x - r_y planar slice of the R_{22} correlation field through $r_z = 0$ after the imposition of walls.

in figure 3-7 is an r_x - r_y planar view through the center of the correlation field, where $r_z = 0$. The solid black line represents the location of the wall.

The correlation field after the wall is inserted requires discussion. Correlations very far from the wall see less effect from the presence of the wall. Correlations close to the wall see much more effect, as demonstrated in figure 3-7. However, care must be taken in performing correlations too close to the wall, because at 1 grid point from the wall, there tends to be more numerical error due to the severe lack of resolution. The

results presented in the majority of this thesis are of correlation results with the correlation being taken at 2 grid points from the imposed wall. Latter results will show the effect of taking the correlations further from the wall, and will be explicitly detailed as to the distance from the wall they were taken.

The grid lines on the image in figure 3-7 are representative of the mesh resolution. The peak value in the middle is still at $r = 0$. The wall in the correlation space is at two grid points to the left, and runs from the top of the image to the bottom, along the x -direction in the image. It is represented by the solid black line in the figure. In the three-dimensional correlation space, the wall would exist in the r_x - r_z plane at the r_y location of $j = -2$.

While figure 3-7 shows the correlation field to the left of $j = -2$ (where the wall is located), the results in that area are not considered physical. By contours levels alone, they are mostly small compared to the important correlation peaks, and in results following these, in an effort to analyze the output after the walls, any information to the left of the wall location is ignored.

It is clear in comparing the pre-wall R_{22} correlation to its post-wall counterpart, that the velocity field acting perpendicular to the wall and its resulting correlation is greatly affected by the presence of the wall. The overall magnitude of the peak of the correlation is nearly halved, and the symmetric oval, or “submarine” shape (in three dimensions) is severely altered. In this thesis, a model was developed to predict this behavior.

The first attempt to predict the reaction of the correlation to the insertion of the walls was to break up the two point correlations as detailed in section 1.5. The first

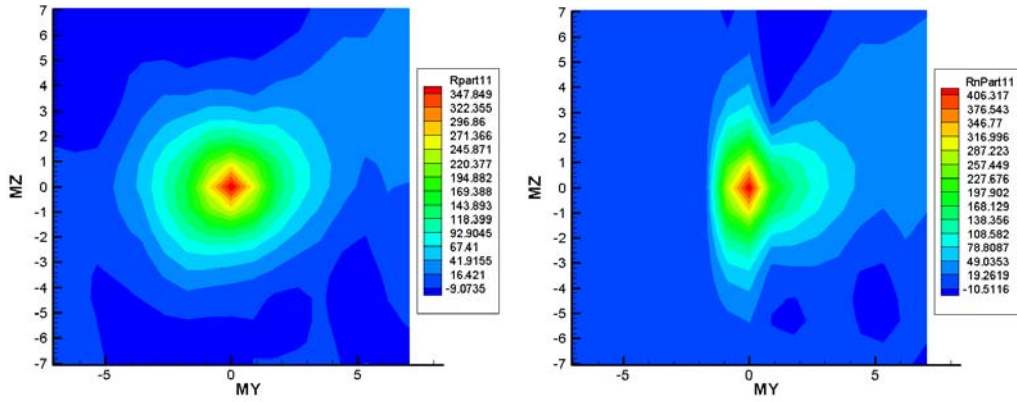


Figure 3 – 8: r_y - r_z plane of the R_{11} Correlation at $r_x = 0$ pre-wall (left), post-wall (right).

correlation that was examined was the R_{11} correlation. The R_{11} correlation was constructed from its constituent parts. The pre-wall and post wall condition for R_{11} are shown in figure 3-8, and the intermediate parts given in equation (1.7) and again in are shown in figure 3-9.

Figure 3-9 shows a Y - Z plane at $x=0$ of the R_{11} correlation's constitutive parts,

beginning with the $\overline{\frac{\partial p}{\partial x} u_1^n}$ term (left), then the $\overline{u_1^n \frac{\partial p}{\partial x_s}}$ term (middle), and lastly the

$\overline{\frac{\partial p}{\partial x} \frac{\partial p}{\partial x_s}}$ (right). The scale on both the axis labeled "MY" and "MZ" is in cell units, and

the contour scale is the correlation values.

The purpose of decomposing the correlation was to gain an understanding of what portions of the decomposition have the most profound effect on the development of the correlation. After performing the decomposition in the code, and summing the constitutive parts together in the correlation space, it was confirmed that the parts sum to the total. This validated the decomposition method. Figure 3-10 shows the difference in the correlation values between the pre-wall condition shown in figure 3-6 and the post-wall condition shown in figure 3-7, for R_{22} . In examining figure 3-9, it was

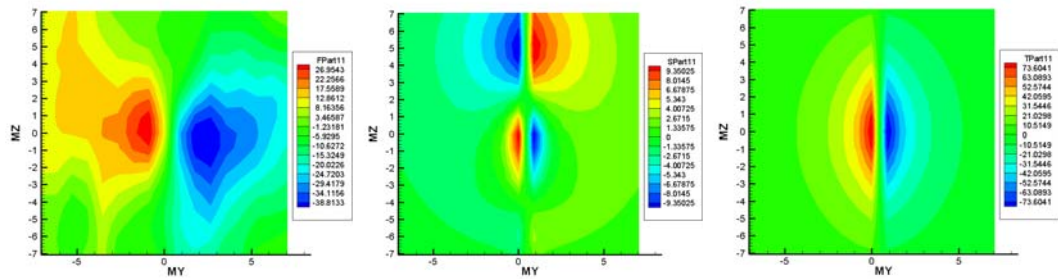


Figure 3 – 9: r_y - r_z plane at $r_x = 0$ of the R_{11} correlation's constitutive parts. The first part (left), second part (middle), and third part (right).

determined that the third part of the correlation decomposition had the highest impact on the final correlation field, as it was the largest in magnitude of the constitutive parts, and was symmetric, making it the ideal candidate for further investigation in this study, as it seemed the easiest to model. This approach did not produce definitive results for R_{11} but did lead to interesting results for R_{22} . After pursuing the decomposition method of predicting the correlations, we determined that it would be better to compare the summation of the constitutive parts to the overall difference between the pre-wall correlation and the post-wall correlation.

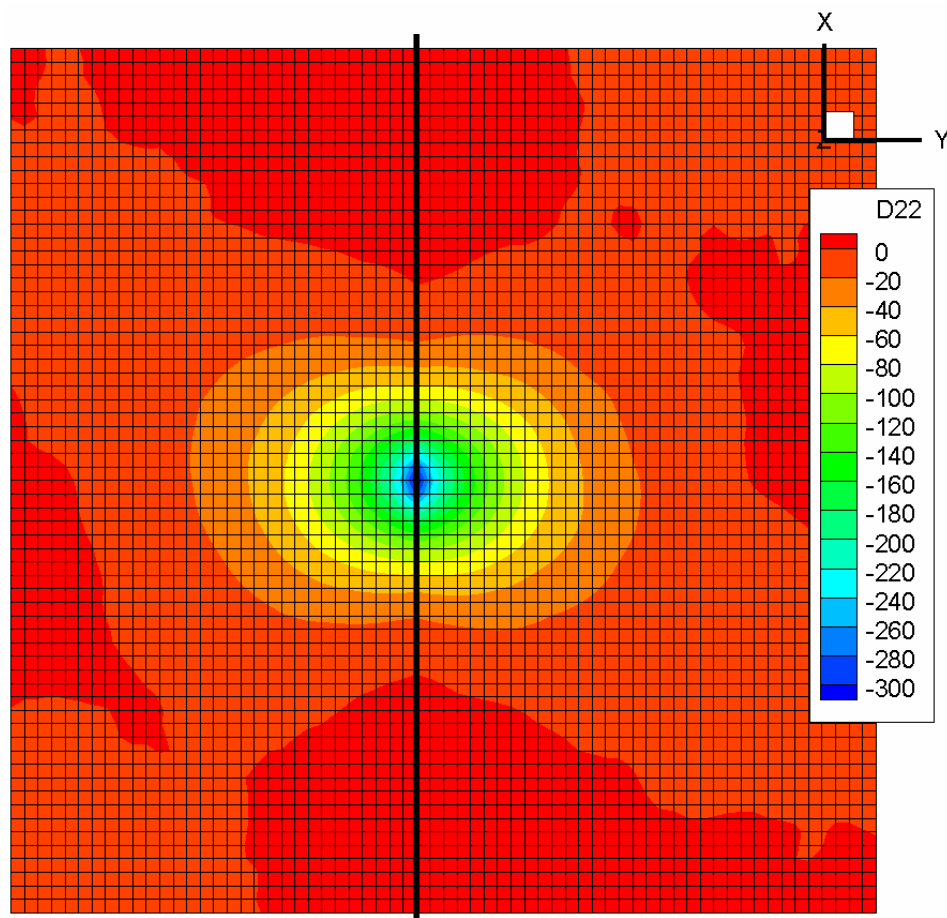


Figure 3 – 10: r_x - r_y Plane at $r_z = 0$ of the difference between the R_{22} before and after the insertion of the wall.

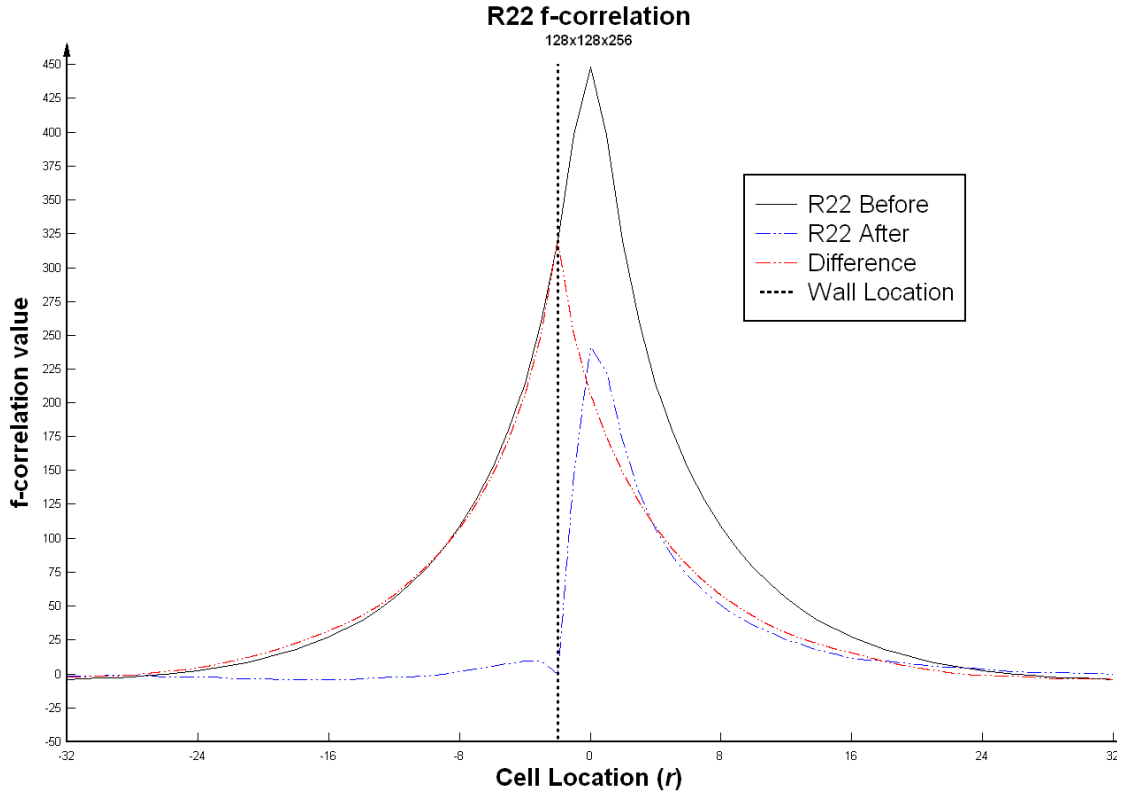


Figure 3 – 11: R_{22} f-correlation with the difference between the two wall conditions plotted.

In performing this difference, the resulting field was surprising. The field of the difference of the two correlations was very similar to the original correlation developed but shifted to the left. The solid black line in the image represents the location of the wall. The original correlation was centered two grid points to the left. In an effort to fully comprehend these results, f-correlations were performed of the correlation fields, and are shown in Figure 3-11.

In this image, the wall was inserted two grid points to the left, and is represented by the thick dotted black line. The dotted red line shown in figure 3-11 represents the difference between the two correlations. It was believed that this shape could be achieved by a scaled down version of the full R_{22} correlation. However, in scaling down the R_{22} correlation, the resulting shape was not similar to the difference.

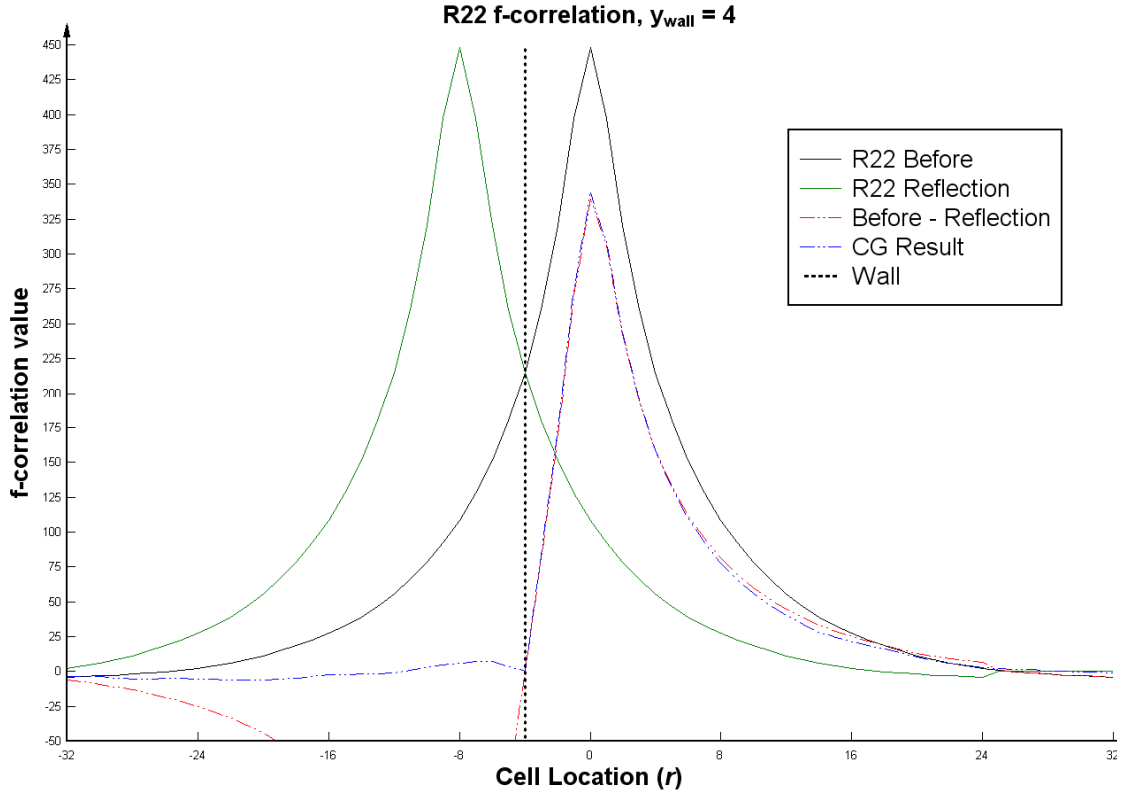


Figure 3 – 13: R_{22} f-correlation with the mirrored and shifted R_{22} correlation plotted, and the resulting difference and actual R_{22} result after the wall. The wall is 4 cell locations from the center of the correlation.

The next attempt at predicting the final R_{22} correlation was to subtract a mirrored and shifted R_{22} correlation. The R_{22} correlation was shifted twice the wall distance, y_{wall} , which is the distance from the correlation center to the wall. This is shown in figure 3-12. The process of mirroring and shifting the correlation shall be referred to as the reflection technique.

The reflection technique does not account for the behavior beyond the wall. Beyond the wall (to the left), the correlation is zero (theoretically) and therefore is trivial to model. Figure 3-12, demonstrates this discrepancy.

The reflection technique predicts the near wall correlation behavior exceedingly well. In an effort to further analyze the reflection behavior, the wall distance y_{wall} was

varied to investigate if the technique applies well at any distance from the wall. It is shown in figure 3-13 and 3-14 that the reflection technique also performs well for the conditions where the wall is farther from the center of the correlation field.

The farther from the wall the correlation is taken, the less affect the pressure has on the perpendicular velocity, v . As y_{wall} increases, the reflection technique predicts the correlation behavior more accurately. These simulations were performed at $128 \times 128 \times 256$ resolution, which is in the low DNS range of simulations. At lower resolutions, the reflection technique predicted the behavior less accurately. Therefore, with increased resolution of the near wall behavior, the reflection technique performs better.

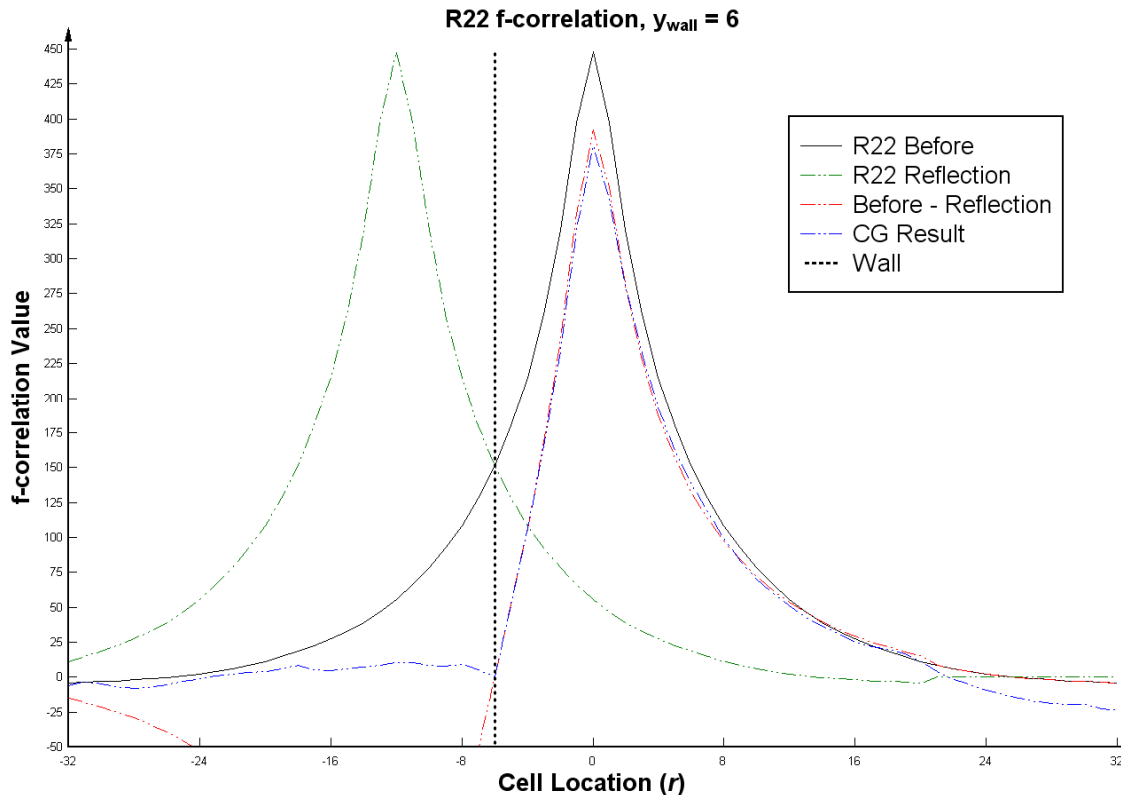


Figure 3 – 14: R_{22} f-correlation with the mirrored and shifted R_{22} correlation plotted, and the resulting difference and actual R_{22} result after the wall. The wall is 6 cell locations from the center of the correlation.

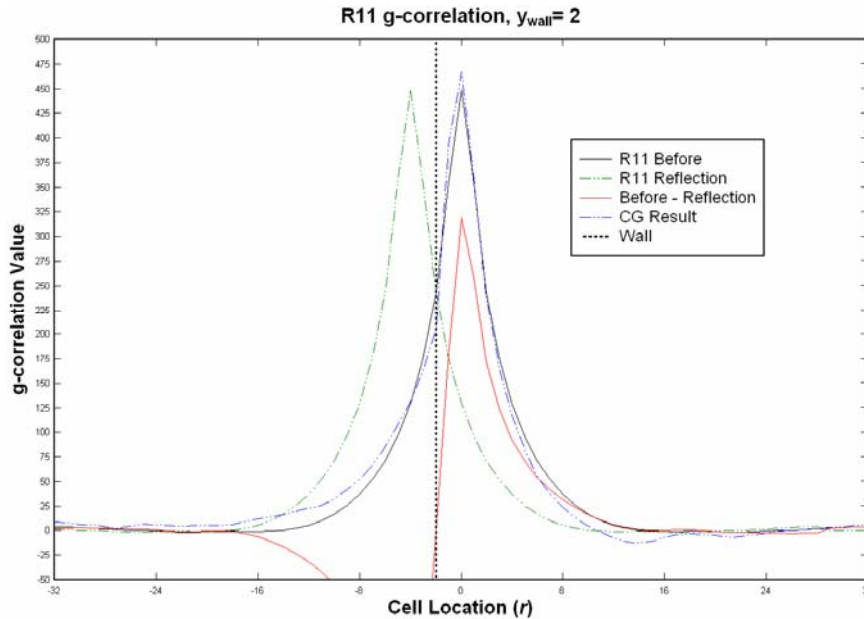


Figure 3 – 15: R_{11} g-correlation with the mirrored and shifted R_{11} correlation plotted, and the resulting difference and actual R_{11} result after the wall. The wall is 2 cell locations from the center of the correlation.

Similar analysis using the reflection technique was performed for all R_{ij} configurations. It was discovered that the reflection technique predicted the correlation behavior well for all the correlations involving the perpendicular velocity v , but not for any correlations that involved the tangential velocities exclusively. For our study of the walls on the Y faces of the domain, the v velocity was the corresponding affected velocity, and the reflection technique accurately could predict the behavior of the R_{22} , R_{21} , R_{12} , R_{32} , and R_{23} correlations. It could not, however, predict the R_{11} , R_{13} , R_{31} , and R_{33} correlations well. This is shown in Figure 3-15. Here, we examine the g-correlation of R_{11} , as it is the correlation of R_{11} affected directly by the wall. The correlations not predicted by the reflection technique are referred to as “off-correlations”. This is shown graphically in figure 3-16. The highlighted area represents the correlations that are well predicted by the reflection technique.

$$R_{ij} = \begin{bmatrix} R_{11} & R_{12} & R_{13} \\ R_{21} & R_{22} & R_{23} \\ R_{31} & R_{32} & R_{33} \end{bmatrix}$$

Figure 3 – 16: Graphical representation of the reflection technique and the correlations it predicts (highlight).

Figures 3-17 and 3-18 demonstrate the R_{12} correlation, and the reflection techniques applied to it. To begin, the R_{12} correlation does not behave like a characteristic R_{ii} correlation as seen previously. As shown in figure 3-17, it has a characteristic “flower” orientation, with alternating areas of positive and negative correlation about the center of the correlation space. This has its roots in continuity, and conservation of mass. At the center and along the main axis, the correlation should be zero, and the areas in all quadrants around those axes should have alternating correlation values, as shown. Because of this orientation, the plane that contains behavior resulting from the wall insertion is the r_x - r_y plane, about $r_z = 0$. This is shown on the right image. The planar slice is averaged 32 times over various z locations in the domain, thus it has a “smoother” contour image.

Figure 3-18 shows the results of applying the reflection technique to the R_{12} correlation. The wall is two cells away from the correlation, and because of the orientation, everything below the wall is beyond the wall, and therefore non-physical. The resulting part of the correlation matches in both shape and magnitude. This result is similar for the other cross-correlations that involve the perpendicular velocity, v .

The idea behind the reflection technique and its relatively simple prediction is believed to lie in vorticity. Vorticity is easier to understand than velocity because it does not involve the pressure. Vorticity is present in turbulent flows, and when the wall is inserted, the wall boundary condition requires image vorticity to be present on the left side of the wall. This causes the flow to be essentially reflected about the wall.

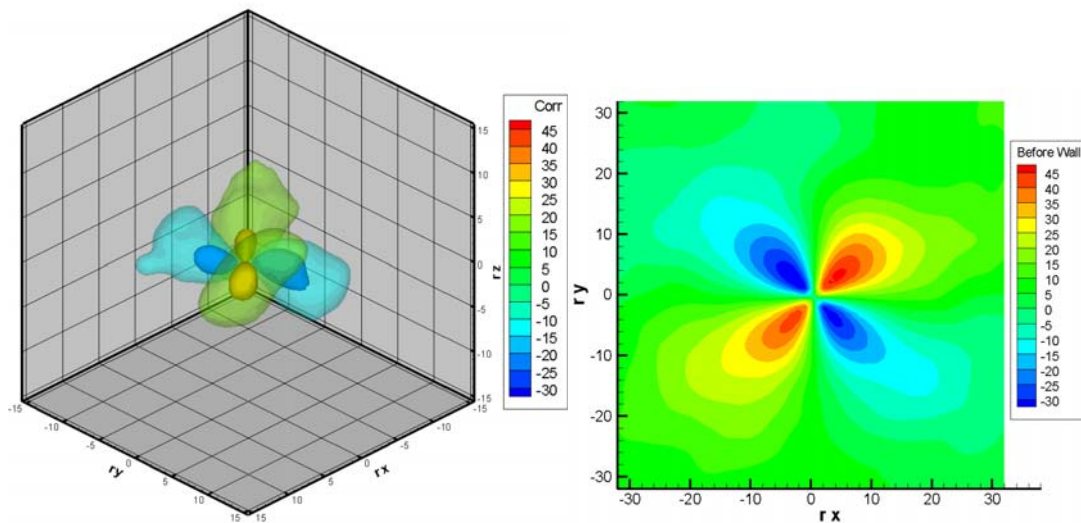


Figure 3 – 17: R_{12} correlation in 3-dimensions (left) and a r_x - r_y planar slice about $r_z = 0$ (right).

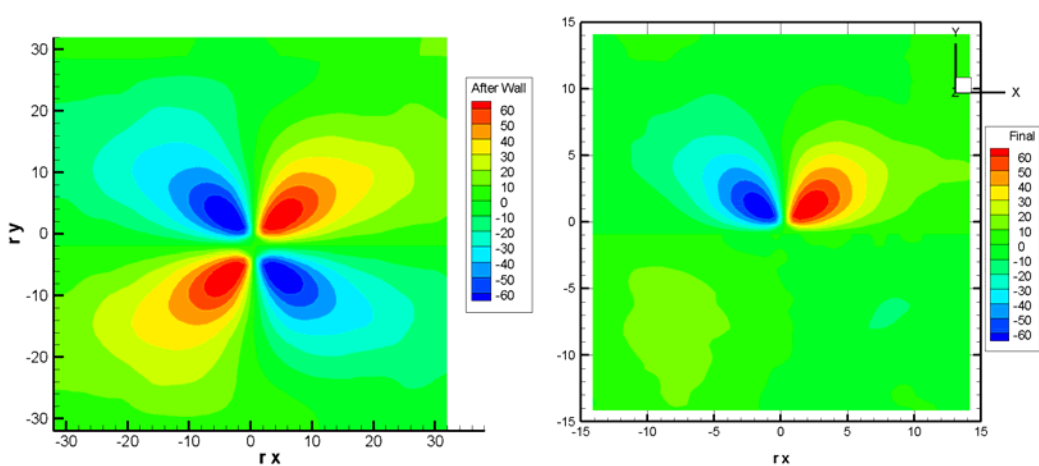


Figure 3 – 18: R_{12} correlation after wall insertion, reflection model (left) and computed (right).

While this works well for flow into and out of the wall, the flow perpendicular to the wall, and its reflection, is less obvious. Determining the wall effect on the parallel velocities posed more of a challenge, and so a vorticity approach was taken.

3.4 Vorticity

Calculating the vorticity is not difficult. Vorticity is the curl of the velocity field, $\omega = \nabla \times u$. Figure 3-19 shows a section of a staggered mesh, with velocities located in the correct location. This figure is the reference to show how the vorticity is calculated.

The calculation used for calculating the vorticity in the x -direction is

$$\omega_x(i, j, k) = \frac{v(i, j, k)\Delta y + w(i, j+1, k)\Delta z - v(i, j, k+1)\Delta y - w(i, j, k)\Delta z}{\Delta y \Delta z} \quad (3.3)$$

The x -vorticity is comprised of the v - and w -velocities, as well as the cell spacing between them. The vorticity is calculated about the x -axis centric to all 4 velocities. Because of the staggered mesh, this vorticity is located along the cell edges that intersect centric to the 4 velocities. The red boxes represent the cells one z -direction above the black cells, and the blue cells are one y -location behind the black cells. The vorticity of interest is highlighted in yellow, and the corresponding velocity components are labeled.

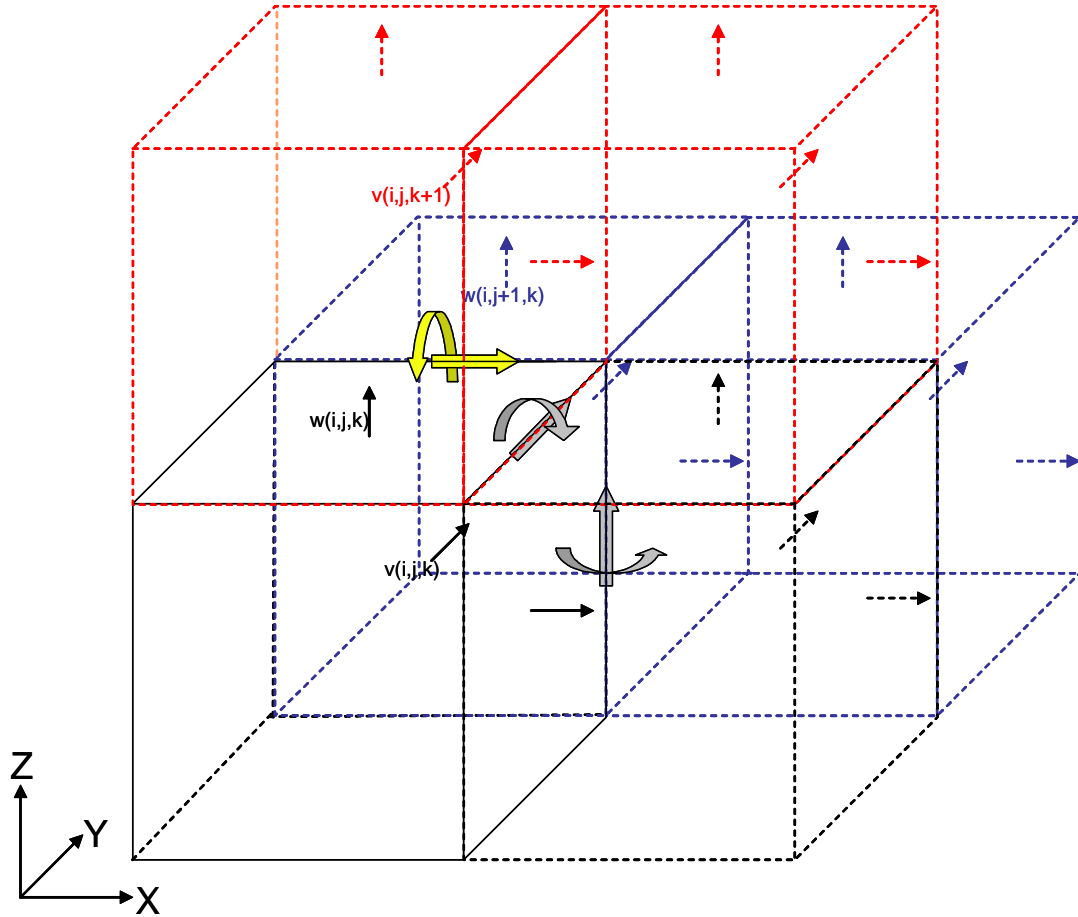


Figure 3 – 19: Vorticity field calculation.

Using this method, and applying it to the other directions, the vorticity fields were calculated. In order to validate the created vorticity fields, the curl of the vorticity fields was examined. Because of incompressibility, the curl of the vorticity is equal to the Laplacian of the velocity,

$$\nabla \times \omega = -\nabla^2 u \quad (3.4)$$

While it is simple to create a valid vorticity field, it is not as easy to calculate velocities from the vorticity field. In the work of this thesis, the vorticity fields that were created were representative of the local velocities immediately surrounding the location of interest where the vorticity was sought. The goal was to modify the vorticity

fields via reflection, and then deduce the velocity field from them. Upon creation of the vorticity field, it should be possible to immediately return a velocity field from the vorticity field identical to the former velocity field. This did not prove as simple as it would seem.

The first main attempt at constructing a velocity field from a vorticity field was utilizing the Biot-Savart law. Rooted in electro-magnetism, this is a method by which to determine a magnetic-field vector from the magnitude and direction of a source current. The fluid-mechanics parallel is that it can determine a velocity, due to a vortex. The Biot-Savart equation in terms of fluid mechanics is given in equation (3.5).

$$\bar{u}(\bar{x}) = \frac{1}{4\pi} \int \frac{\bar{\omega} \times (\bar{x} - \bar{x}')}{|\bar{x} - \bar{x}'|^3} d\bar{x}' \quad (3.5)$$

In equation (3.5), $\bar{\omega}$ is the vorticity, and $(\bar{x} - \bar{x}')$ is the distance from the vortex to the velocity field. The integral is a volume integral, over all three directions. This method did not return our initial velocity values.

The next approach is from a paper by R. Yakota.[16] His method uses a modified Biot-Savart equation that tries to account for the singular nature of the integral.

$$\mathbf{u}_i = \frac{1}{4\pi} \sum \frac{\left(r_{ij}^2 + \frac{5}{2}\sigma^2\right)}{\left(r_{ij}^2 + \sigma^2\right)^{\frac{5}{2}}} (\bar{r} \times \bar{\omega}) \quad (3.6)$$

where $\sigma = c\Delta x$.

This approach was intended to smooth the singular nature of the resulting velocity field due to the finite vortex spacing. Initially, this method was difficult to implement, as the resulting velocity fields that were generated did not match those with which it was supplied. Therefore, validation with simple vorticity cases was necessary in order to prove that this method was appropriate, and to determine c .

In order to validate the results of the modified Biot-Savart method shown in equation (3.6), we applied it to several simple test cases in which the solution can be derived analytically. The first case examined was that of a single line vortex of infinite length.

It follows in the derivation of Katz [17] that after manipulation of this equation and application of the infinite length boundary condition of the vorticity, it falls out that the velocity at a point induced by a infinite vortex is given by

$$u = \frac{\omega_z}{2\pi r} \left(\frac{y}{r} \right) \quad v = \frac{\omega_z}{2\pi r} \left(\frac{x}{r} \right) \quad w = 0 \quad (3.7)$$

In this case, a vortex strength of 100.0 was used. The velocity field should have a $1/r$ behavior as distance from the vortex increases.

For this validation case, the single vortex was generated acting positive in the z -direction, as shown in Figure 3-20. In analyzing the resulting velocity field, a planar slice of the velocity was examined perpendicular to the vorticity, as designated by the yellow highlighted plane in Figure 3-20. The behavior described in equation (3.7) is for an infinite vortex, and the vortex was made “infinite” in the calculation by using periodicity in the vortex direction. It is important to note here that periodicity was not applied in the transverse (x, y) directions, as this would represent many vortex lines acting in parallel.

The modified Biot-Savart equation (3.6) involves the tuning variable, σ . It was initially thought that this was on similar order of the cell spacing, which proved true. However, it became apparent in the examination of the test cases that there resulted in a

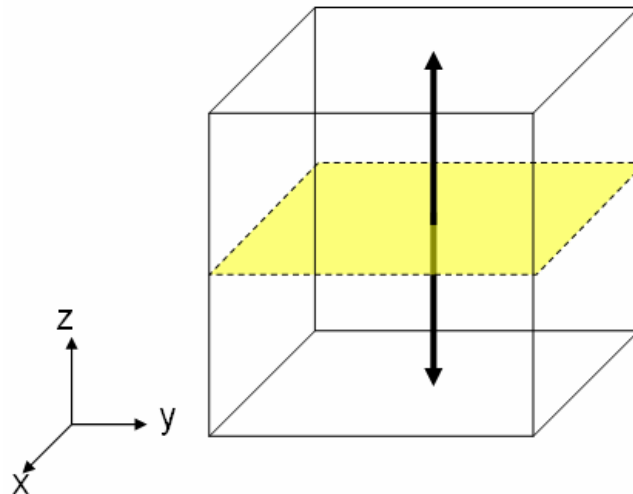


Figure 3 – 20: Diagram of single vortex (black arrow) in a domain.

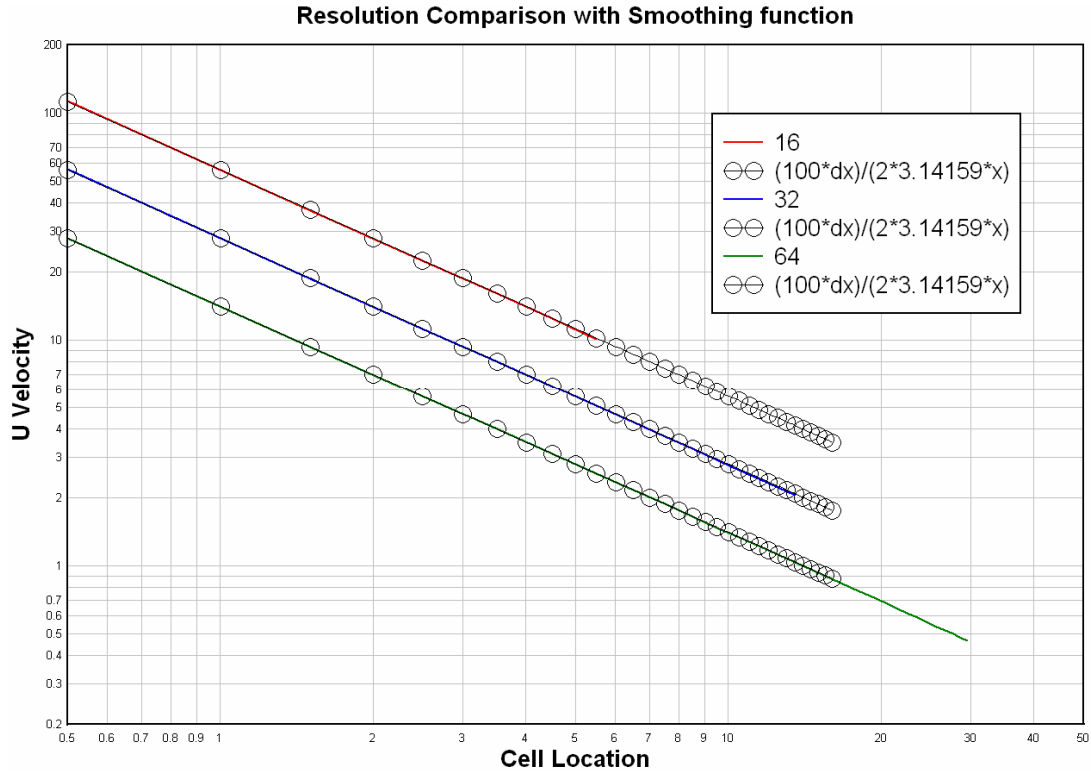


Figure 3 – 21: The velocity associated with a vortex strength of 100 for different resolutions. Theoretical result (colored lines), computed result (circles with solid black lines)

tuning constant being necessary in the calculation of σ , such as equation (3.8).

$$\sigma = C\Delta x \quad (3.8)$$

Numerical calculations, and equation (3.7), produces the expected $1/r$ behavior. However, there is a dependence at very short lengths ($< \Delta x$) of r on the value of the constant C . It greatly affected how the curve at the first and second points closest to the vortex behaved. The best constant C associated with a line vortex was 0.38. With this sigma value, the modified Biot-Savart returned the appropriate $1/r$ dependence, as shown in Figure 3 – 21. With the value of the constant $C = 0.38$, the velocity has the expected $1/r$ behavior as shown with the black circles/line. The red, blue, and green designate different resolutions, showing that the value of 0.38 for C is valid for any resolution.

It is important to note at this juncture the effect of tuning σ . Altering the value of σ greatly affects the velocity field prediction close to the actual vortex. This behavior is important to note, because when predicting the velocity at a point in a turbulent field of vorticity, it is the vorticity components closest to the velocity component in question that have the greatest effect on an accurate velocity prediction.

The second method of validating the modified Biot-Savart method is by simulating a sheet of vorticity. This involves a plane of vorticity, with the vorticity acting in either of the planar directions, but not out of the plane. This is shown in Figure 3-22. The sheet of vorticity is acting in the z -direction, and the velocities are those on the x - y plane denoted by the yellow sheet. The physical velocity condition that would produce such a vorticity field would be planar shear, with two velocities acting equal and opposite in the x -direction along a plane, and constant beyond that plane.

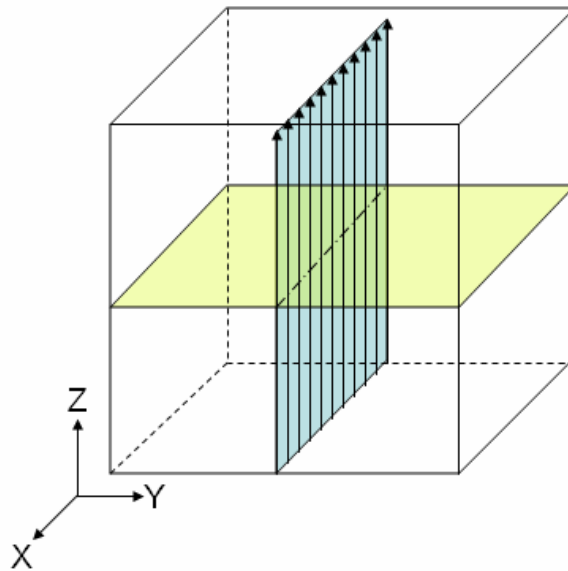


Figure 3 – 22: Diagram representing the case of a planar sheet of vorticity (blue) in a domain.

In this case, a vorticity sheet with a vortex strength of 100.0 was created. The parallel velocities to this sheet are easy to derive from this vortex strength, as the velocities on either side of the sheet are constant. From the definition of the calculation of the vorticity, it can be shown that the exact solution is -88.35 at the left of the vortex sheet, and +88.35 on the right.

Using the numerical Biot-Savart law on this test case produces the expected velocity field, but only to an extent. As with the line vorticity, the solution generated by the modified Biot-Savart requires manipulation of the σ constant in order to correct the near-vorticity velocities. It was discovered in performing this validation that the value of σ in order to produce the expected result was different than that of the single line vorticity. The value of C required in the planar vortex sheet is close to 0.5.

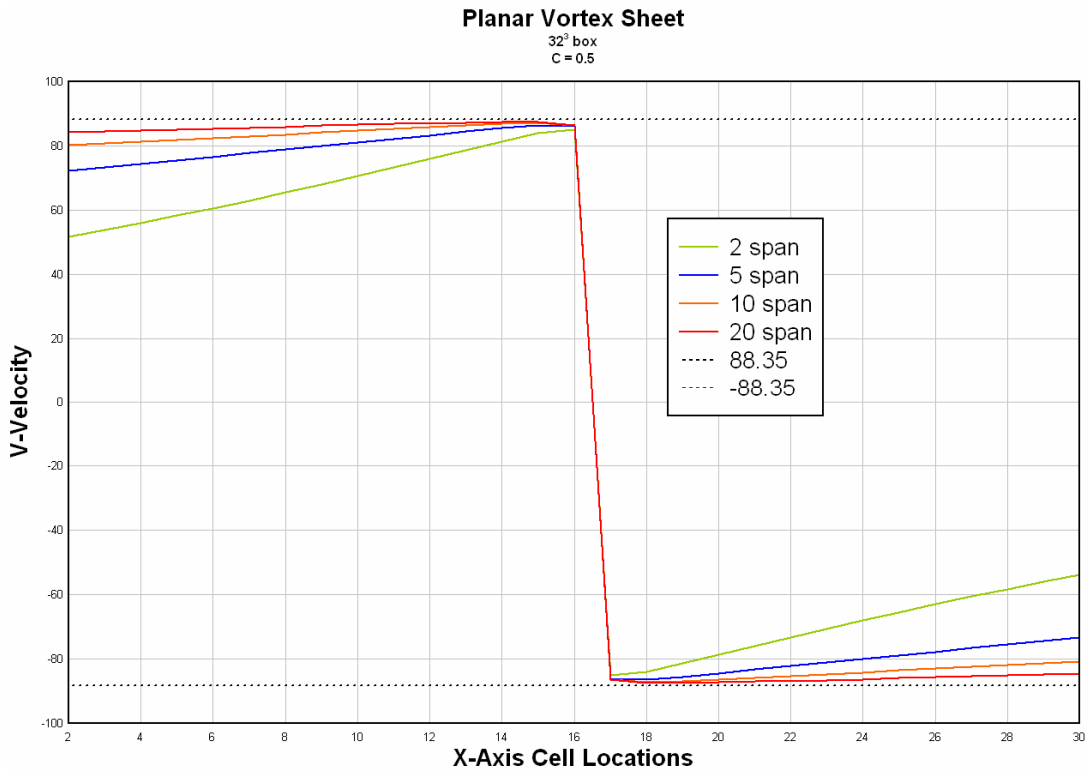


Figure 3 – 23: Planar Velocities as a result of a vortex sheet.

The planar sheet case also emphasizes the importance of the span used when performing the numerical Biot-Savart. Figure 3-23 shows the results of the planar case taken with different spans, with the constant value $C = 0.5$. While in theory it would be best to use an infinite span to arrive at the correct solution, there exists a steep cost in computational time and resources that incurs with an increase in the span. Therefore it follows that there is a span where the error between the result and the expected result is acceptably small, with the knowledge that with infinite time and computational resources, the solution would improve.

One last validation case that was examined added a level of complexity to the velocity prediction. The resulting velocity fields, both graphical showing span dependence (a) and magnitude vectors indicating magnitude and direction (b), are shown in Figure 3 - 24. While more of a test case than validation, it was designed to

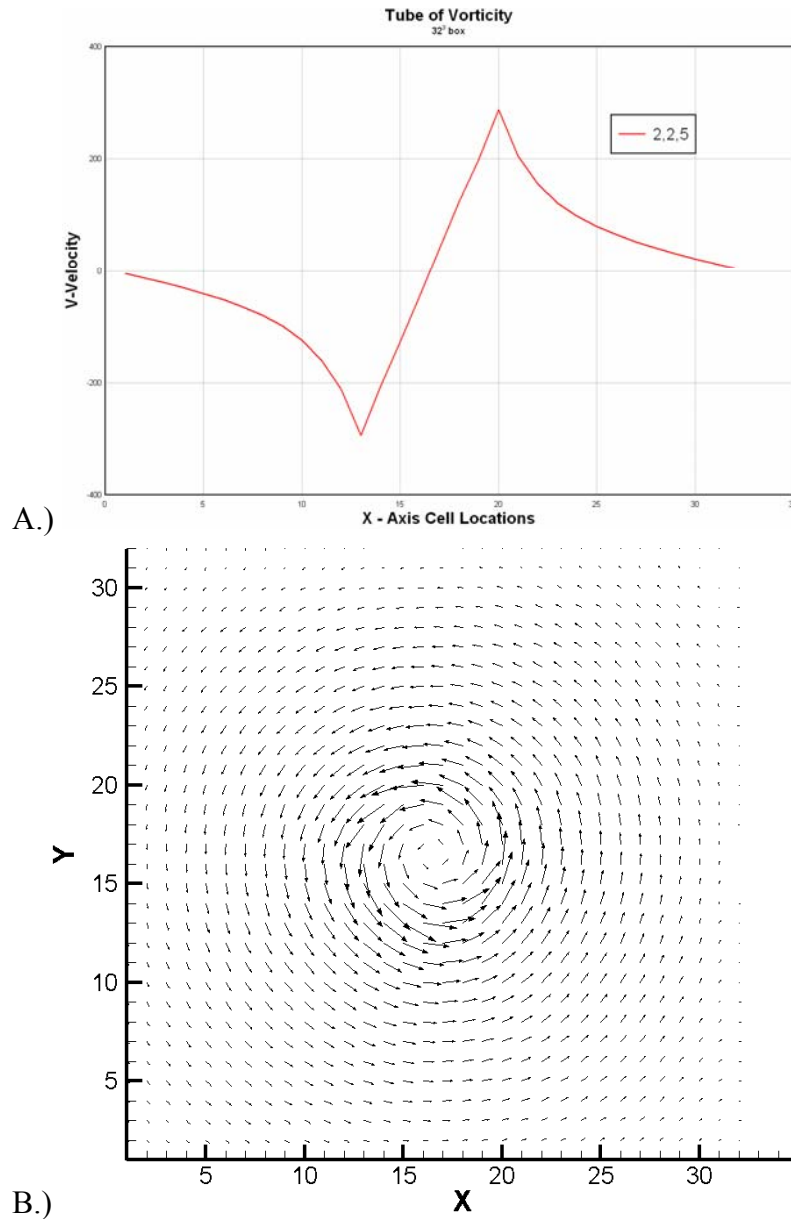


Figure 3 – 24: Tube of vorticity results. A.) V-velocity along a line in the x -direction. B.) Velocity vectors showing both magnitude and direction.

examine how well it would predict the result of a common phenomena, that of a vortex tube. Commonly approximated in nature in examples of solid body rotation, it consists of a tube of constant vorticity acting in the direction of the tube. Such a condition produces a linear velocity profile within the tube, and a $1/r$ decay profile at and beyond the outer wall of the tube.

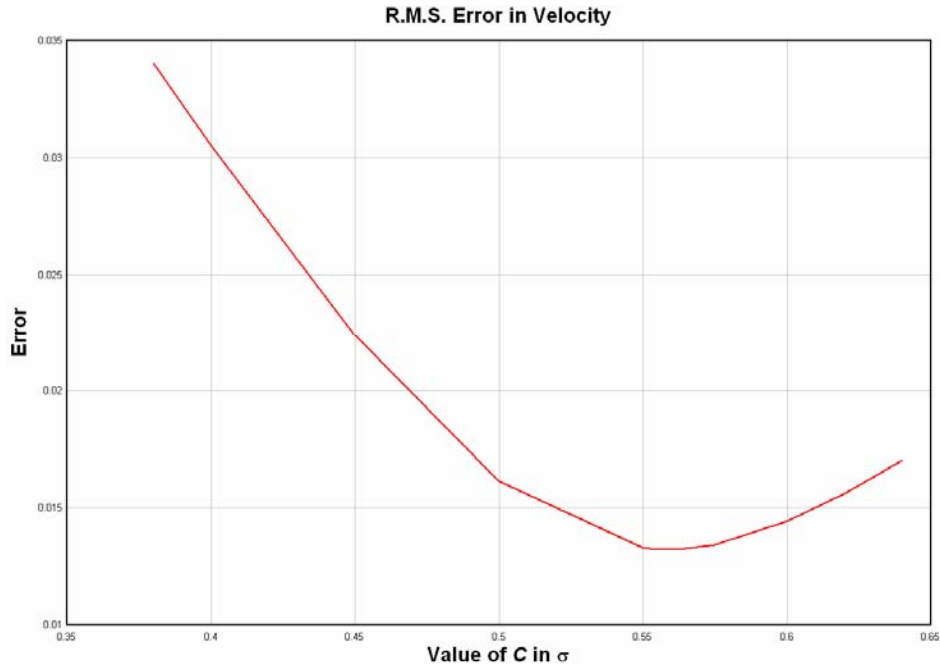


Figure 3 – 25: Error resulting from different values of C in the calculation of σ .

Finally, the numerical Biot-Savart method was applied to vorticity fields developed from actual velocity fields. Initially it was believed that the value of σ should be between two values experienced by the line and planar vorticity cases. However, this proved not to be the case, as using an arbitrary value between the two yielded fairly significant errors between the resulting velocity field and the field that was used to generate the vorticity field. It was determined that the value of the constant C that generated the closest solution to the supplied velocity fields was 0.5575. This was determined by examining the root mean square error between the initial velocity field and the Biot-Savart calculated velocity field. As shown in Figure 3 - 25, it reaches a minimum at the value of 0.5575. This value was thought to be appropriate, as it could be conceived that with increasing complexity of the vorticity field, the value of C in σ increases as well. The value of 0.5575 is also close to the value of $\frac{\sqrt{3}}{\pi}$ which makes σ box diagonal length over π . This observation holds for this simulation only, because an

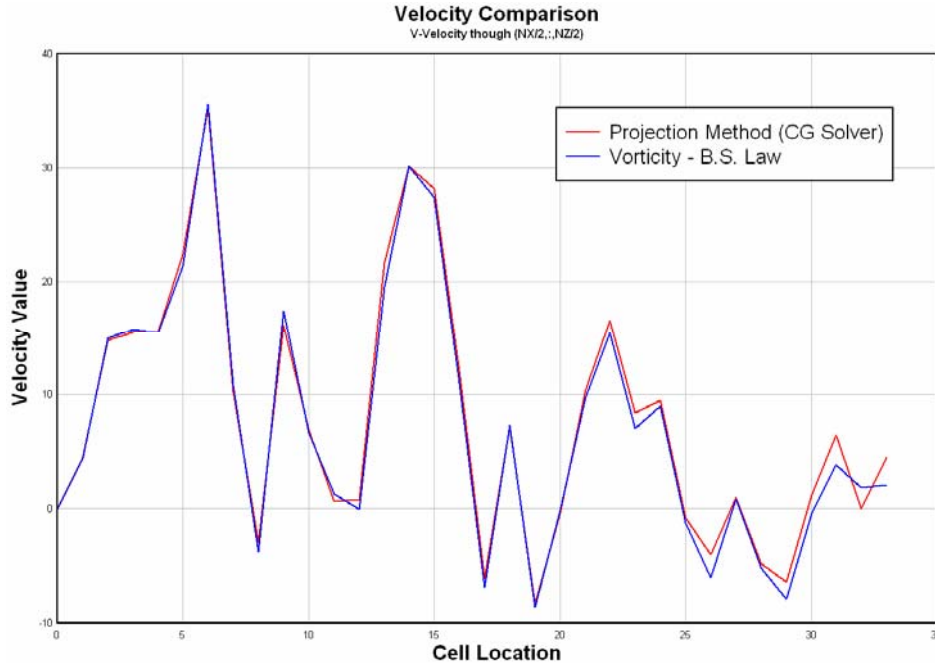


Figure 3 – 26: Velocity comparison of the actual resulting velocity field and that generated from the vorticity.

uniform mesh size was used, where $\Delta x = \Delta y = \Delta z$. It is not known if this relationship extends to non-uniform meshes.

A span study was performed, to investigate the influence of the span used in the velocity field. While the solution did improve with increasing span size, its effect was small compared to changing the value of σ . Because the time it takes to perform the Biot-Savart method scales cubically with the span size, the span used in the following calculations is $32 \times 32 \times 64$. Figure 3 - 26 shows results of the modified Biot-Savart method, showing a line of velocity through the turbulent field. It is worthy to note that this comparison is of v-velocities generated after the implementation of the wall. The red line is the resultant velocity field after the wall was applied using the projection method, and the blue line was from the modified Biot-Savart Law, described above.

With the ability to generate velocity fields from vorticity fields, it is now possible to examine how alterations of vorticity fields affect the velocity results. More

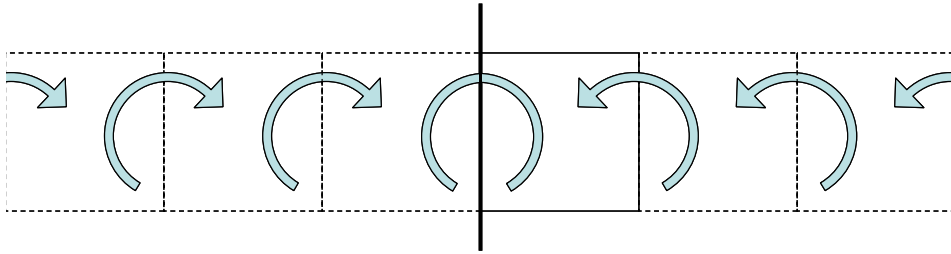


Figure 3 – 27: Reflected, semi-periodic domain.

specifically, it is possible to modify the vorticity field as is expected in the presence of the wall, and generate a velocity field result. The presence of the wall induces image vorticity on the other side of the wall, and per our model explained earlier in this thesis; we can modify the vorticity beyond the wall to represent this. When implementing this, it produces similar results to those generated by solving the Navier-Stokes with the wall boundary conditions. This comparison is shown in Figure 3 - 26.

By altering the modified Biot-Savart method, we can examine the vorticity contributions to the predicted velocity. The idea is to examine the contribution from the vorticity on the flow-field side of the wall, and the contribution from the vorticity beyond the wall. This is shown by the illustration in Figure 3 - 27. The original domain is outlined by the solid black square, and periodic domains are outlined by dashed lines (more on that later) Looking at Figure 3 – 27, the vorticity to the left of the wall (solid black vertical line) would be in one summation, and the vorticity to the right of the wall would be a separate summation. By performing separate summations of those groups of vorticity, it becomes easy to determine the effect of the wall, and how far into the flow field it acts.

It is important to note the nature of periodic vorticity fields employed when performing these summations. As shown in the above figure, the left hand side (beyond

the wall) vorticity is the reflection of the original domain, but only with vorticity that has a component perpendicular to the wall. In the case of the wall acting in the x - z plane, the vorticity acting in the x - and z -direction would both be reflected and negative of on the other side of the wall. However, the y -vorticity would be only reflected. The sign remains unchanged, since it contains velocity components parallel to the wall, and thus the wall boundary condition has no effect on it.

Once the wall boundary condition is applied to the vorticity fields, they are made periodic, but only on either side of the wall, as shown in Figure 3 - 27. All of the domains beyond the wall are periodic in and amongst themselves, up to the wall. All of the domains on the original side of the wall are also periodic among themselves, up to the wall. For the cells at the wall, the boundary condition that is set there is that the vorticities containing wall-perpendicular velocities (ω_x, ω_z) are set to zero because of the wall boundary condition. For the purposes of this simulation, the vorticity containing only wall-parallel velocities (ω_y) was left unaltered at the wall.

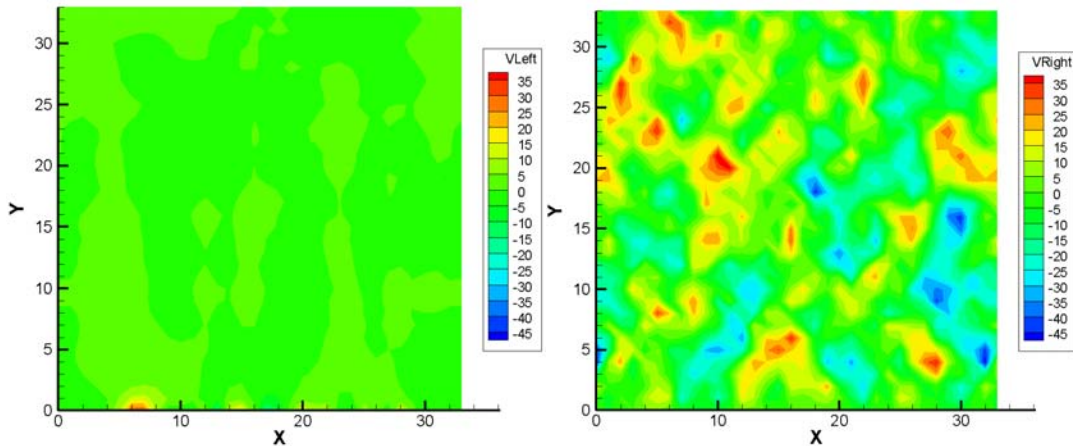


Figure 3 – 28: The v -velocity contributions from the vorticity beyond the wall (left image), and contributions of the vorticity to the existing side of the wall (right image). The wall is located at $Y = 0$.

Figure 3-28 shows a slice perpendicular to the wall of the v -velocity, the left image being that of the beyond-the-wall vorticity contributions, and the right image being the velocity contributions from the flow-field on this side of the wall.

Performing these split-summations, it allows us to decompose the correlations and our proposed correlation model in order to see which contributions have the greatest effect in the development of the after-wall condition. Using the notation ‘left’ to refer to the velocity contributions from the vortices beyond the wall, and ‘right’ to denote the velocity contributions from vorticities on this side of the wall, we can perform correlations of the right-right (RR) velocities, the left velocity contributions correlated with the right velocity contributions (LR), the counter right-left correlations (RL), and the two beyond the wall contributions, left-left (LL). These should all sum up to the full correlation field, as shown in equation (3.9). These correlation contributions are shown in figure 3-29.

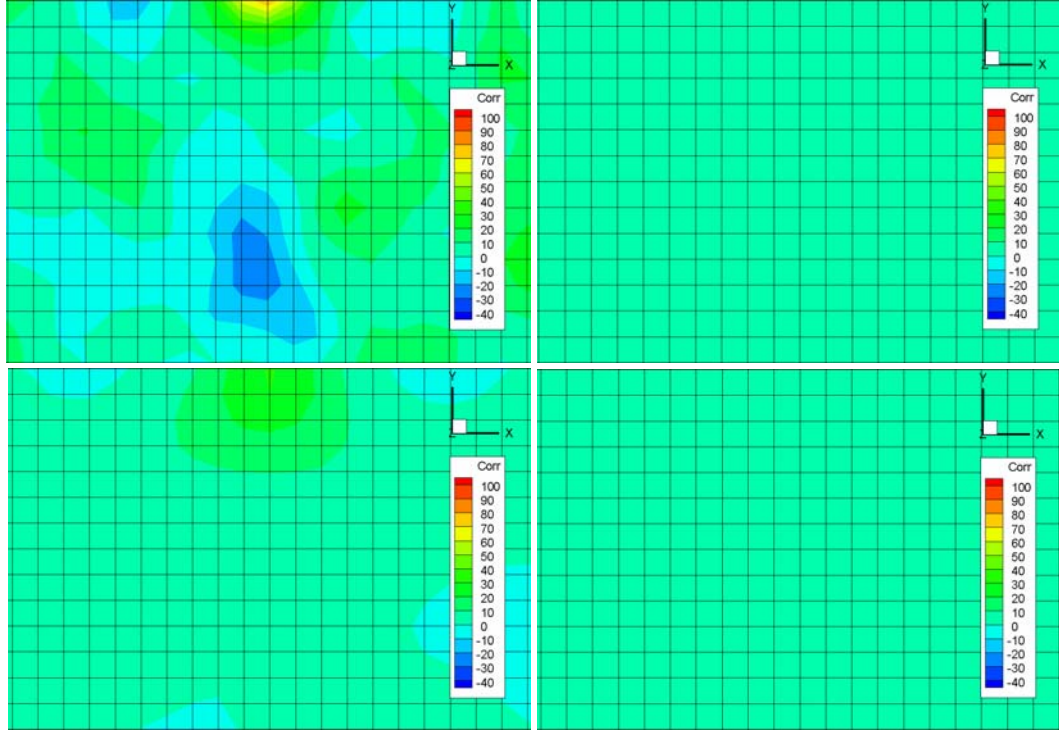


Figure 3 – 29: Decomposition of the correlations. Clockwise, from top left, the RR correlation, the RL correlation, the LR correlation, the LL correlation. In each image, the wall is located at the top.

$$R_{ij}(\bar{x}_1, \bar{x}_2) = \frac{\overline{u_i^{right}(\bar{x}_1)u_j^{right}(\bar{x}_2)} + \overline{u_i^{right}(\bar{x}_1)u_j^{left}(\bar{x}_2)} + \overline{u_i^{left}(\bar{x}_1)u_j^{right}(\bar{x}_2)} + \overline{u_i^{left}(\bar{x}_1)u_j^{left}(\bar{x}_2)}}{2} \quad (3.9)$$

Planar slices of these constitutive correlations are shown in Figure 3-29. In performing these correlations, it is of interest to examine the parts of the correlations from before the implementation of the walls that are involved in the predictive model covered earlier in this thesis. Looking at Figure 3-12, it is of interest to examine what constituent correlation parts contribute to the red line, denoted as ‘difference’, that alter the original correlation to yield the resulting correlation due to the wall. In examining what part of the correlation contributes to this part, it is clear to see that original correlation, beyond the wall location, is what comprises the ‘difference’. In examining the constitutive parts of the correlations performed before the addition of the walls, and

blanking out the values that do not contribute to the ‘difference’, and interesting development arises.

As shown from Figure 3-29, the only correlations that affects the predictions of the after-case or those that are correlated with the flow field-side of the wall. In each image, the wall is at the top. Therefore, these are the contributions from the correlations that would comprise of the reflected portion that modifies the original correlation to produce the after-wall correlation condition. Any correlations performed that involve contributions from beyond the wall have little effect on the final solution, as their contributions are two or more orders of magnitude small than the others.

3.5 Low Reynolds Number Strain Flow

This section highlights the efforts spent in determining why some of the low strain rate cases performed by Jay Gadebusch were not as expected when comparing against the results of Hallbäck. While his results for the higher strain rate axisymmetric contraction cases followed closely the results of Hallbäck, the lower strain rates did not. These cases are of interest for their ability to tune turbulence models. When these peculiar results came to light, analysis was performed using the initial conditions from Professor De Bruyn Kops work[2].

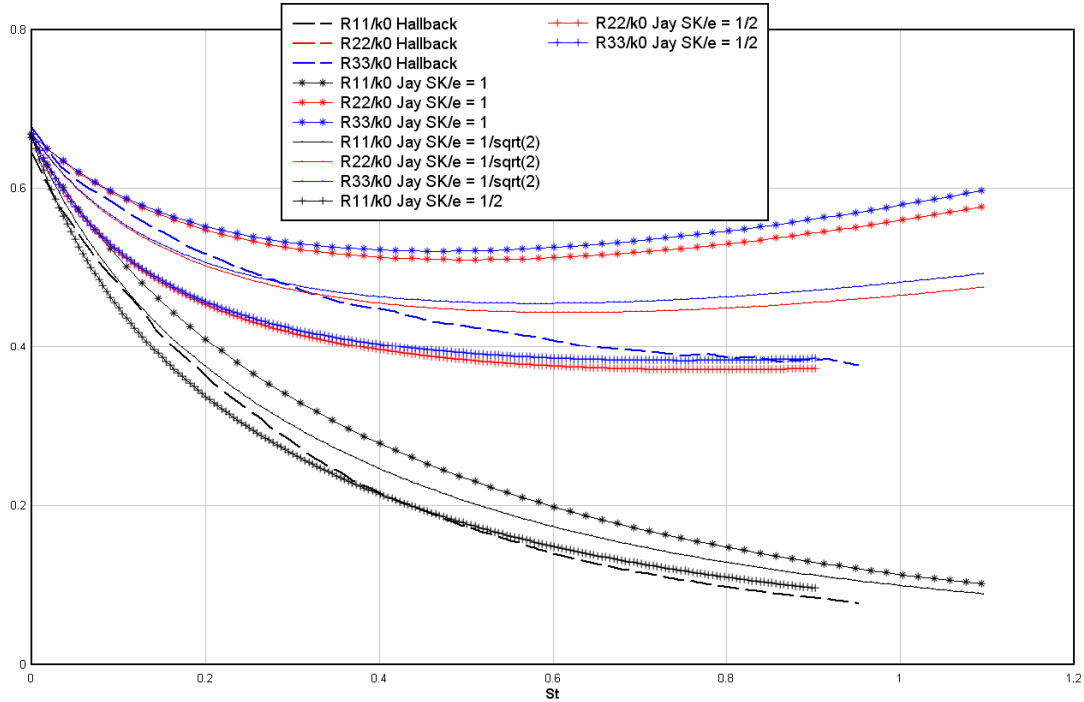


Figure 3 – 30: R_{11} , R_{22} , R_{33} , normalized by the initial kinetic energy versus non-dimensional time, St .

It was initially thought that there was a misinterpretation of the definition of the strain rate, and that it was off by a factor of 2, or $\sqrt{2}$. In Hallbäck and this work, it was used that $S = \sqrt{2S_{ij}S_{ji}}$. Figure 3-30 shows the efforts of this investigation. The dashed lines represent the data from Hallbäck, and the solid lines represent the data from the simulations performed by Gadebusch.

It is shown in figure 3-30 that while it was initially suspected the strain rate was the cause of the low strain rate issue, it did not solve the problem. At this point, the focus shifted onto the initial conditions being used. Having noticed the “skewness” from work with the two-point correlations, it was thought that a slight inherent shear in the initial velocity fields might cause the axisymmetric contraction cases to not agree with Hallbäck’s data at low strain rates. As the strain rate decreases, the results would show an increased effect of the inherent strain in the flow, even if it was small in

magnitude compared to the strain applied to the flow. At the smallest strain rate, the effect of the inherent strain might be substantial enough to cause a noticeable change in the results, compared to agreement with Hallbäck's data.

An investigation into the initial conditions was performed, using the full $768 \times 768 \times 1536$ fields, looking at planar averaged velocities in the z -direction. The results of this analysis are shown in figure 3-31. While the global average velocity is equal to zero, the individual planar averages are not, as shown in the figure. Furthermore, it is believed that there can almost be drawn a periodic oscillating line through the average velocities that would indicate a shearing between the upper half of the domain (in the z -direction) and the lower half of the domain. In order to account for this fact, Gadebusch had averaged both the top and bottom half of the domain, and that average was subtracted from both halves respectfully. This introduced strain into the field, and in turn may have been the cause behind the discrepancy between the agreement of Gadebusch's results and those of Hallbäck in the high and low strain rate cases.

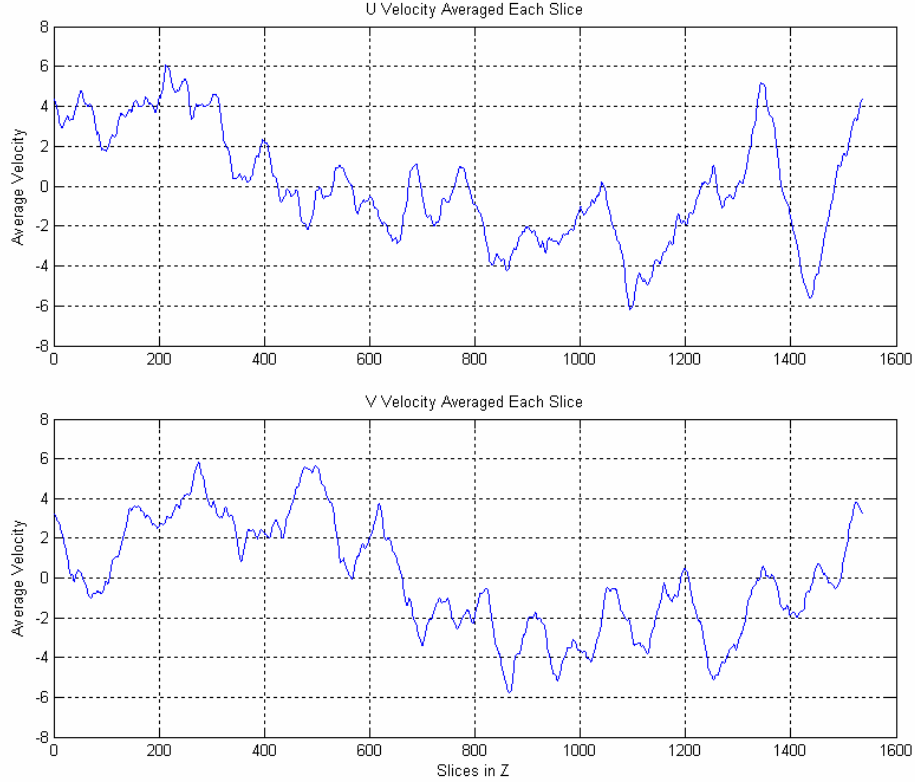


Figure 3 – 31: *XY*-Planar velocity averages of the *u*- and *v*-velocity fields in the *z*-direction.

In an effort to account for the cuboid structure of the domain without introducing the strain associated to two large averaged values being subtracted across the mid-*z*-plane, it was attempted to find a continuous function in the form of equation (3.10) to subtract off from the fields. This function would be made periodic in the domain, to ensure that on average no velocity was leaving the box, thus ensuring incompressibility.

$$\left(A \cos\left(\frac{2\pi z}{L}\right) \right) - \left(B \sin\left(\frac{2\pi z}{L}\right) \right) \quad (3.10)$$

In the above equation, L is the length of the domain. A and C were empirically determined, based off of the FFT of the planar averaged velocity fields, A is based on

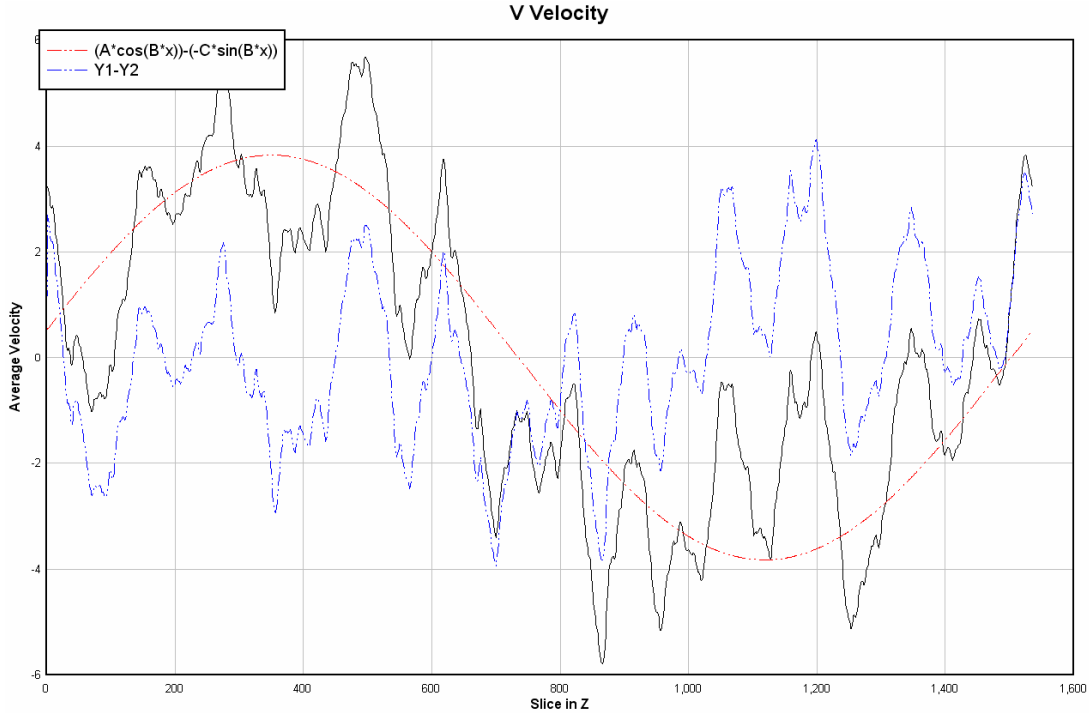


Figure 3 – 32: Planar velocity averages of the v -velocity fields in the z -direction (solid), the correcting function (red dashed), and the resulting corrected profile (blue dashed)

the real component, and C is based off of the imaginary component of the first wave number (the lowest frequency oscillating mode). The results for the v -velocity alteration are show in figure 3-32. The dash-dotted line has this lowest mode removed.

The value for the real component A in this case was 0.33108, and the imaginary component B was 2.414665. While this improved the fields, it did not improve the Hallbäck results or the skewness in the two-point correlations. It was at this point that new initial conditions were desired to be created.

3.6 New Initial Conditions

The first attempt at the generation of turbulent initial conditions was the randomly located and oriented jets in a domain, as described in section 2.4. While this

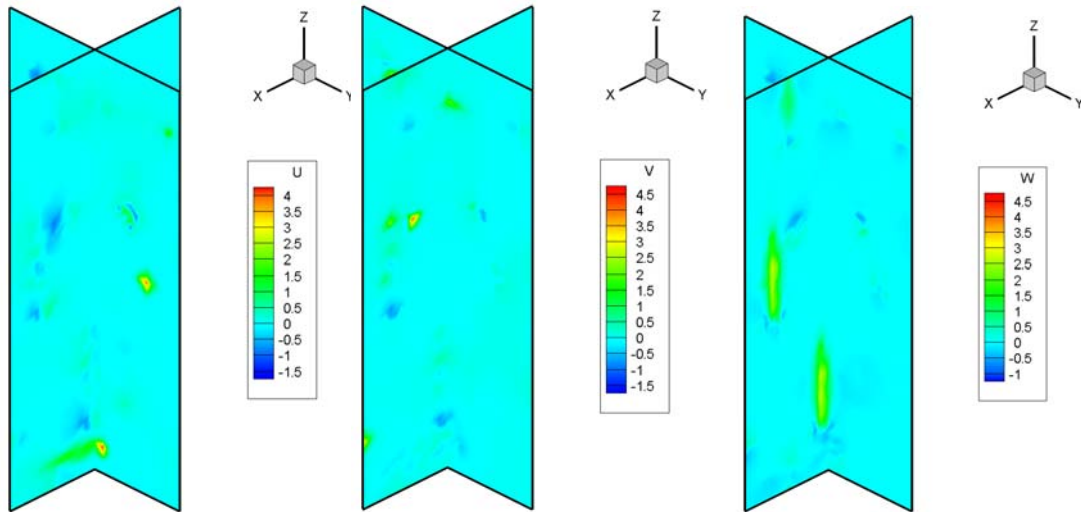


Figure 3 – 33: Cross sections of velocity fields showing the u , v , and w velocity fields, from left to right, respectively.

method generated fairly isotropic fields, it lacked the physically realizable generation that was desired. The jets were only 1 cell in diameter, and as the domain increased, the effects of the jets decreased. Figure 3-33 shows some early results of the jets .

As the jet fields progressed in time, jets would turn off and new jets would turn on, thus increasing the randomness of the flow within the domain. The flow in the domain is periodic, such that there are no complicated boundary conditions due to any walls.

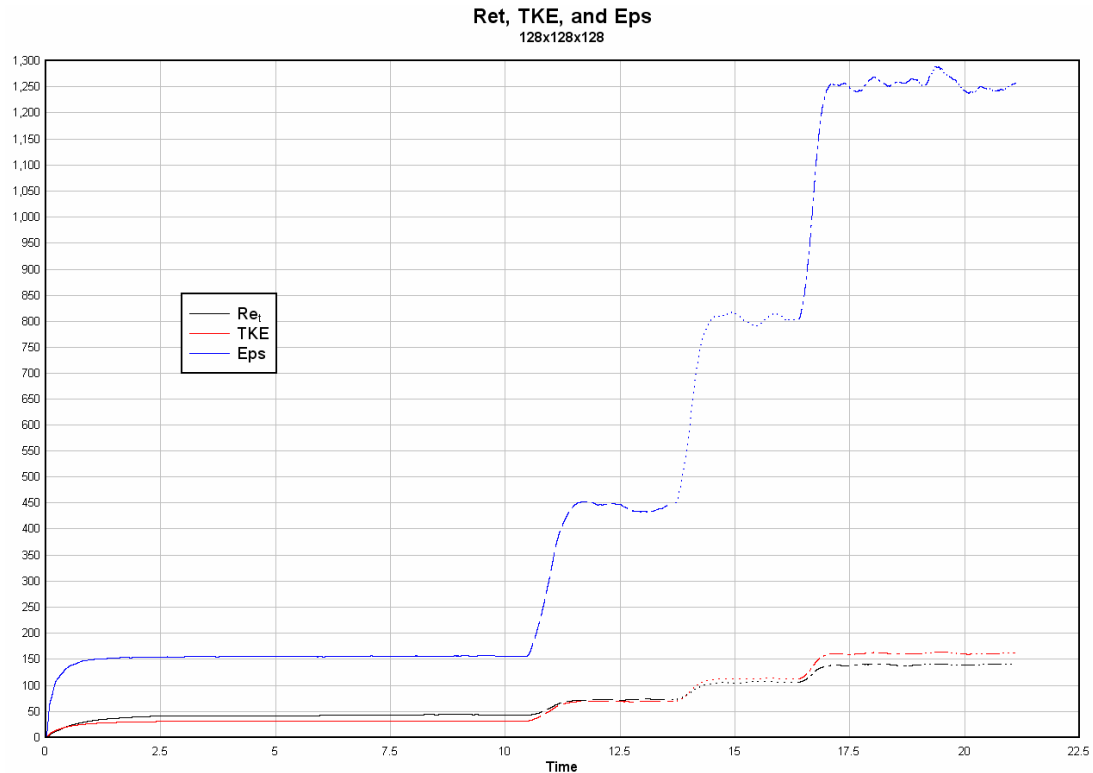


Figure 3 – 34: Turbulent Reynolds number (Re_t), Kinetic Energy (TKE), and Dissipation (Eps) vs. time (in seconds).

As mentioned above, while the jets were mildly successful in generating initial fields, they failed to develop in to fields resembling figure 1-1 as the domain size increased. However, as expected, there were promising trends that led to development of the box technique. These trends included the increasing of the turbulent Reynolds number of the flow as time progressed and the mixing continued. An example of how the turbulent Reynolds number, the kinetic energy, and the dissipation evolve in time is shown in figure 3-34. Each “step” is due to a higher jet acceleration being imposed.

In the figure, the different styles of dashed lines indicate different run sequences of the field generation. For the initial time period (solid) the acceleration of the jets was set for a low value, around 2000 cm/s. The second initialization of the flow, started from the restart files of the first run (thick dash), had a higher acceleration, of 4,000 cm/s. This resulted in a higher turbulent Reynolds number, kinetic energy, and

dissipation. For the third (thin dotted) and fourth (dash-dotted) continuations of the field, the accelerations was increased to 6,000 cm/s and 8,000 cm/s respectively. Both increases in acceleration of the jets yielded increases of all three turbulent flow characteristics, as shown.

While the jets did not result in exactly the flow fields that were desired, they yielded insightful results. An important lesson learned was the necessity of a method for checking the location of the jets, and ensuring that new jets were not placed too closely to other jets. Having jets placed too close to other jets create areas of diverging flow, which would lead to un-desirable or non-physical results.

After moderate success in the creation of fields using randomly oriented jets, a different and more physically realistic method was considered. A field of stationary solid boxes is randomly allocated in a domain. The boxes have no-slip boundary conditions, and are impermeable. A pressure driven flow is then introduced and forced past the field of boxes for a set amount of time in a random direction. A pictorial example of what the domain looks like is shown in figure 3-35.

In going about generating these new initial conditions, a varied number of parameters needed to be set. These parameters include the number of boxes, the size of each individual box, the magnitude of the pressure driven acceleration of the flow, and the time duration of the pressure driven flow in any particular direction. All these different variables combine to produce a field of turbulent flow.

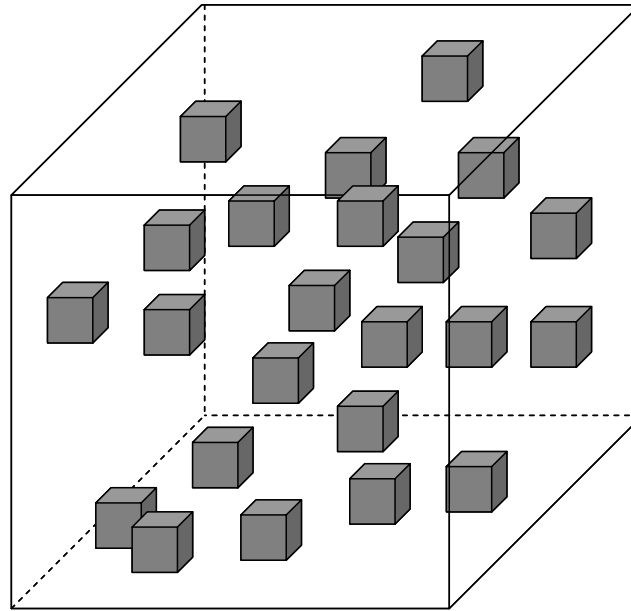


Figure 3 – 35: Simplified diagram of flow field with cubes placed randomly inside.

To begin with, the number and sizes of the boxes in the flow are related, in the sense that too many boxes or boxes too large in magnitude would not produce desirable flow characteristics. As this code is parallelized, these parameters are global parameters. For the initial conditions generated in this thesis, the number of boxes chosen is 1000, with each box being 5 grid points cubed. In the fields generated, which are 128 x 128 x 256 grid points in dimension, this means that the boxes placed in the fields account for close to 3% of the total domain volume. The boxes are evenly spread out among each sub-domain and are randomly positioned within each sub-domain in order for a random distribution of boxes to be ensured in the entire domain.

This brings up an important note regarding the nature of random number generation in a parallel environment. When using the inherent random number generated within the Fortran libraries, it makes use of a seed number to determine where in its explicit list of random numbers it should begin. In order to truly

‘randomize’ the numbers chosen by the random number generator, it is possible to call a seed randomizing function that chooses a seed value based on the date and time the function was called. While this is an intelligent function to use in serial cases, issues were encountered in the parallel environment. When running the code, the inherent seed randomizing function would be called on each processor within such a small timeframe that it would return an identical seed number for most, if not all of the individual sub-domains. This led to the development of the boxes being put in locations that were identical sub-domain to sub-domain, leading to the flow field being nearly periodic within the domain, which is not desirable.

The random number generator operates by using two seed values to produce random numbers with a period of 10^{18} , resulting in a field of uniform distribution between 0 and 1. The first of the two integer seed values can be set between 1 and 2,147,483,562. The second integer seed value can have the values between 1 and 2,147,483,398. The use of these two seed values ensures that the random number generator is initialized by two 31-bit seeds.[14, 15]

In order to prevent the parallel environment from generating identical seed numbers across different processors, separate ‘seed lists’ were created *a priori*. Each ‘seed list’ contained 512 random number pairs generated at different times. These numbers would serve as the seed for the sub-domains. Each sub-domain would call its corresponding seed, i.e. sub-domain numbered ten would use the tenth number pair on the list as its seed value. This method ensures that no two sub-domains are similar in their box distribution.

With the boxes set in the flow field, the generation of initial conditions can begin. The initial period involves the flow passing over and around the boxes. The initial conditions developed ran for 5.0 seconds, with the pressure gradient changing direction every 0.5 seconds. This was deemed suitable time for the boxes to cause the formation of structures in the flow by the time the flow next changed.

After the flow has been progressing for the 5 seconds, it becomes necessary to terminate the pressure gradient. Upon doing so, the flow is still permitted to flow past the boxes within the flow, and it slows down with the removal of the pressure gradient.

After that time, for the purposes of this thesis, the field was allowed to decay in an effort to examine the decay exponent, covered later in this section. At this point, the boxes are removed from the flow, and replaced by zero-velocity fluid. The flow characteristics at this point are dominated by decaying isotropic turbulence, which allows for the determination of the decay exponent.

At the time of this thesis, the code has reached a level of development that domains of any cubic size and desired turbulent Reynolds number can be created. Modification of the kinematic viscosity is the primary method of altering the flow characteristics of interest, such as the kinetic energy and turbulent Reynolds number. Other methods that produce similar results would be increasing the pressure gradient applied to the flow, or modifying the number of boxes.

An example of the resulting initial condition fields are shown below in figure 3-36. The field is isotropic and divergence free. The method of how the fields were created is quantifiable. The flow has many different scales associated with it, from the pressure driven flow creating large scale structures that drives the small scale

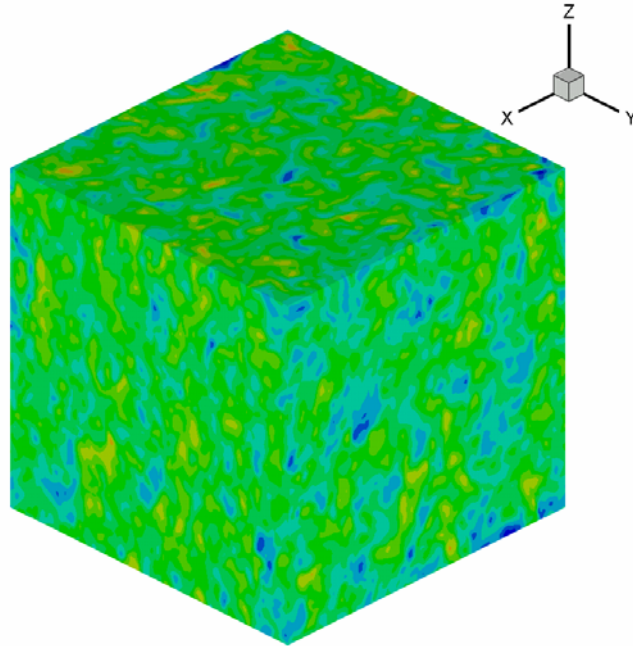


Figure 3 – 36: Full field of u -velocity contours.

dissipation. These traits are shown through the kinetic energy present in the flow, and the dissipation, shown later. The initial conditions have a range of turbulent Reynolds numbers, from about $Re_T = 49$ to $Re_T = 113$.

Two-point correlations were performed on the initial conditions. The three correlations shown in figure 3-37 each were performed on separate initial conditions, and show two important results. The first is that while each two-point correlation could be considered skewed slightly in one direction or another, on average they are uniformly isotropic. The second important result is that the two-point correlation generated by the box method is less skewed than the original initial conditions used previously in this work.

One last comment on the development of the new initial conditions is how the turbulent characteristics develop over time. Unlike the initial condition generation using the jets, the imposition of boxes in the alternating pressure driven flow produces

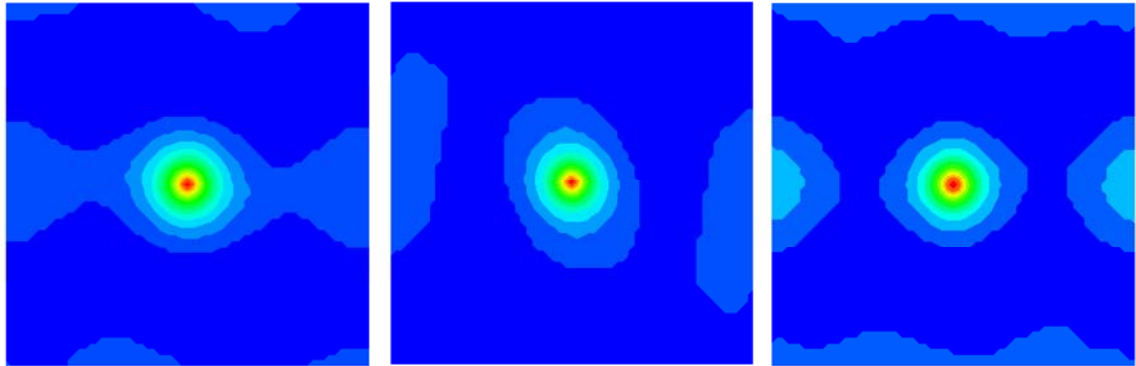


Figure 3 – 37: Resulting R22 Correlations, looking at a X - Z slice in the center of the correlation field.

much more violent swings in both the energy production and dissipation. This is to be expected, because of the nature of the developing flow. When the flow changes direction, you would not only have the tiny structures still in the flow from the previous direction, but you would also be creating new structures resulting from the flow past the boxes in the new flow direction.

3.7 Decay Exponent

In analyzing the development of the initial conditions from physically realizable conditions, it is of interest to examine the decay exponent. Figure 3-38 shows the results from nine different runs, using different flow orientations, averaged together. While this figure may seem noisy, it serves to highlight the widely varying value of the decay exponent for each instance of turbulent flow.

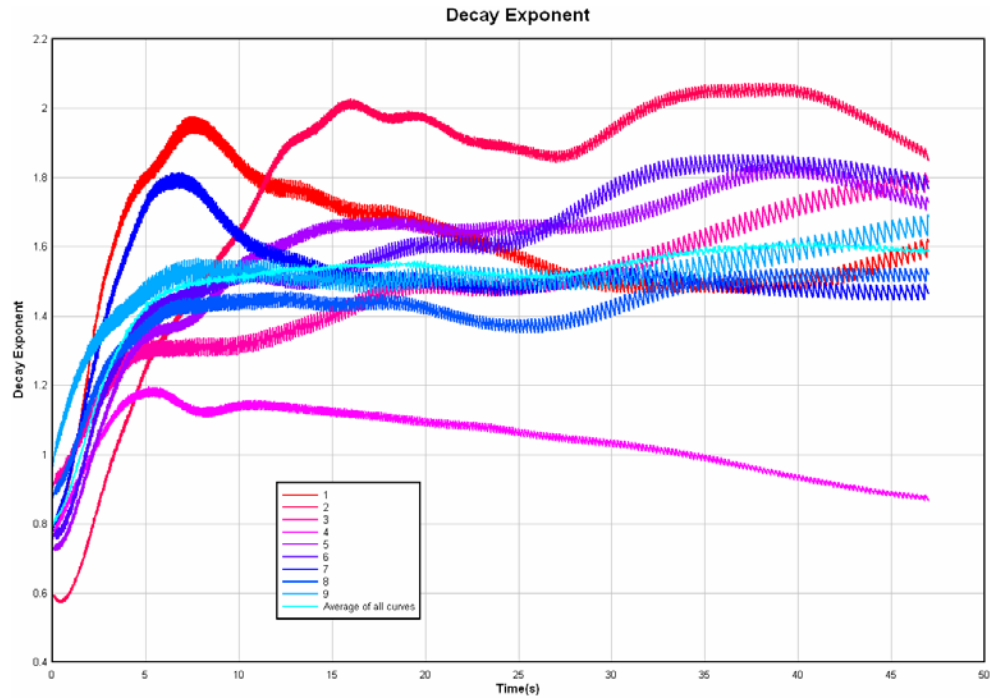


Figure 3 – 38: Decay Exponent, n , vs Time (s) of various initial conditions decaying.

The field was generated for a total of 5.0 seconds, and then it was allowed to relax and adjust for the removal of the pressure-gradient driven flow, and then decay afterwards. Initially, the remaining flow fills in the scattered volumes where the boxes had been, creating an initial spike in energy and dissipation, which promptly ends after approximately 3.0 seconds, depending on the initial condition. As the flow begins to slow down due to energy transfer from the larger scales of motion to the smaller scales, and then to heat dissipations, the decay exponent hovers around the high Re limit of 1.2, and then increases to a value around 2.0, which is the box-constrained limit.

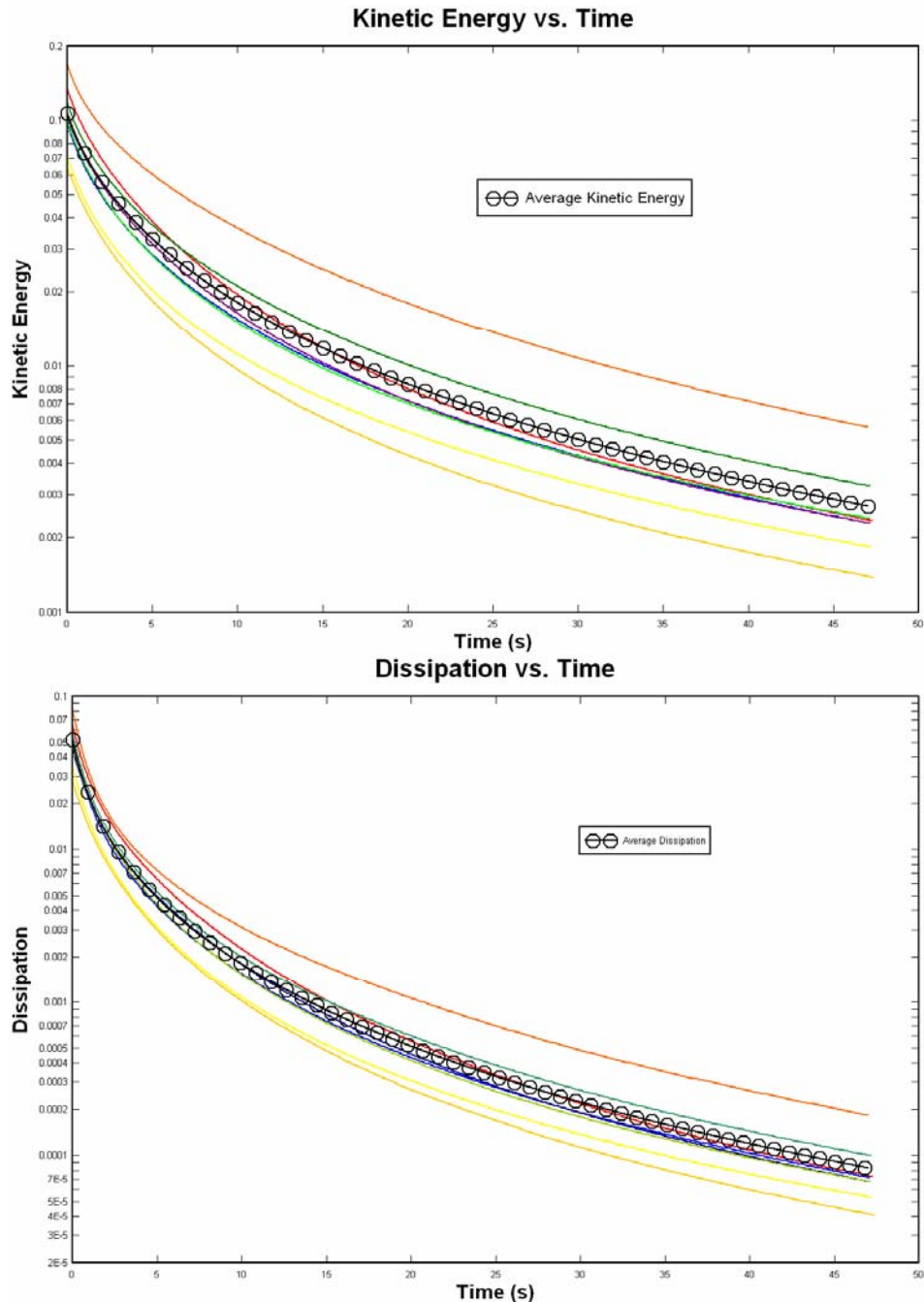


Figure 3 – 39: Kinetic Energy vs. Time of decaying flow (top); Dissipation vs. Time of decaying flow (bottom).

When looking at the decay exponent, it is important to consider average the turbulent characteristics of the flow. As with most turbulent properties, it would be foolish to consider the results of a single instance of turbulence. Averaging the flow using various methods and techniques has much more significance, and is done often

when trying to characterize turbulence. Therefore, it is important when examining the decay exponent that an average of all the flows is generated. However care must be taken when performing this average, and what is averaged in what order. Previously in the thesis proposal, the decay exponent was averaged amongst four different decay exponents, taking the average at each instant in time.

While this was deemed an appropriate method at the time, it was later revisited, and the more appropriate method is to average the relevant raw turbulent statistics, the kinetic energy and the dissipation. The kinetic energy vs. time for each initial condition in its decay period is shown in figure 3-39. Also shown in figure 3-39 is the average of all of the kinetic energy.

Figure 3-39 also shows the dissipation present in each initial condition, and the average of each, versus time. From the averaged kinetic and averaged dissipation, the

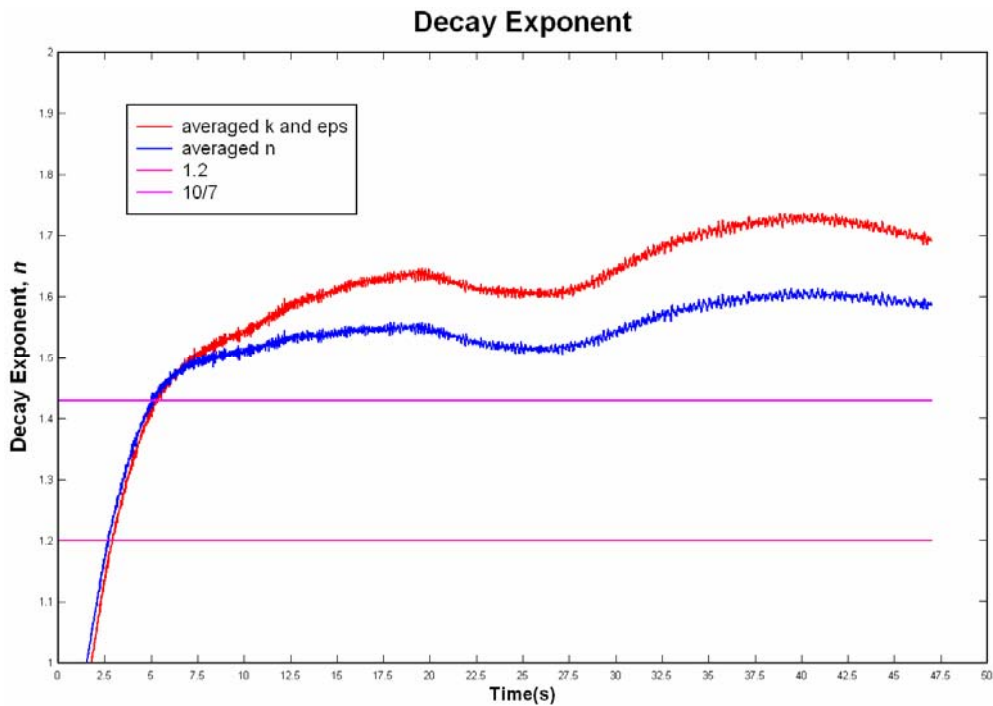


Figure 3 – 40: The decay exponent vs. time, showing the difference between the averaging schemes. The theoretical k^2 and k^4 limits for high Reynolds Number decay are shown by the fuchsia lines.

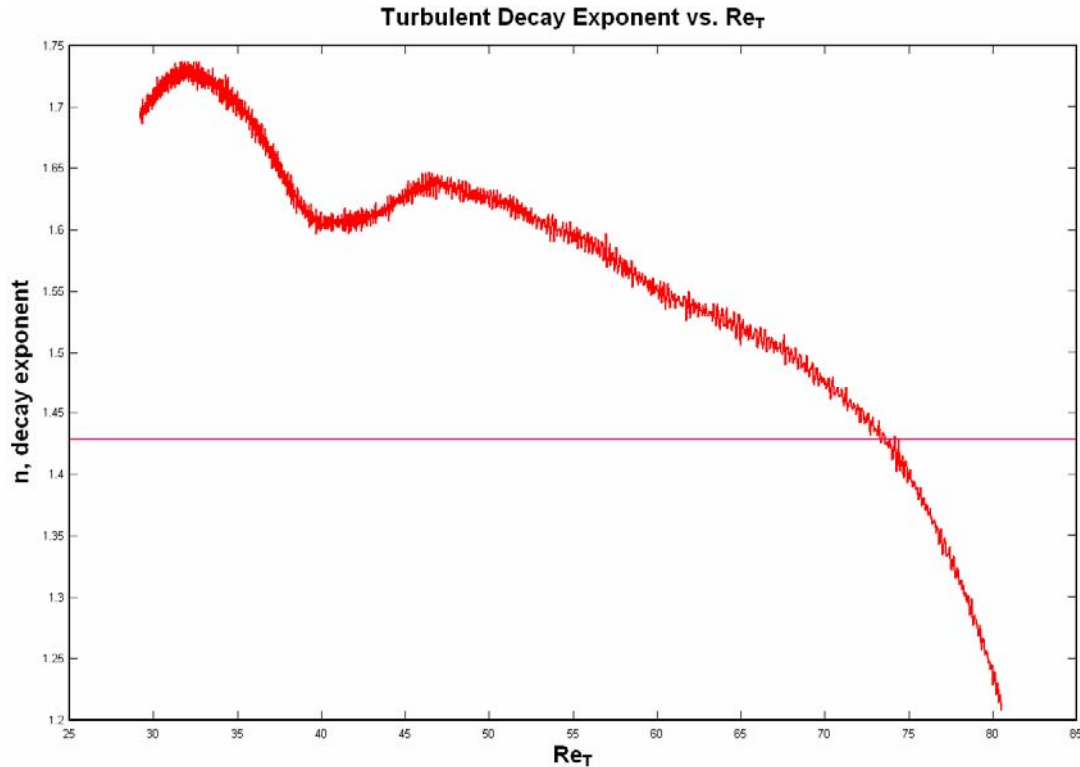


Figure 3 – 41: The turbulent decay exponent vs. Turbulent Reynolds Number. The theoretical k^2 and k^4 limits for high Reynolds Number decay are shown by the fuchsia lines (1.2 is the bottom limit of the figure).

average turbulent Reynolds number is calculated for the decay period, as well as the average decay exponent. It is important to note the difference in performing an average of the turbulent statistics instead of the final decay exponent, and this is shown in figure 3-40. The resulting decay exponent from averaging the turbulent characteristics is higher than simply taking the average of each decay exponent at each point in time Also in the figure are the theoretical limits for both the k^2 and k^4 limits for high Reynolds number decay.

It is now possible to look at how the turbulent decay exponent varies with the turbulent Reynolds number. This is shown in Figure 3-41. As would be expected, the decay exponent is lower in the higher Reynolds number regime, and has a high value in the lower Reynolds number regime. The main characteristic of importance, however, is

that it does not appear to asymptote towards any particular value, as the theory would suggest. This brings forth an important consideration in regards to the turbulent decay exponent. It may be the case that attempting to reduce decaying isotropic turbulence to a single value may prove to be an overzealous simplification. In knowing exactly how the initial conditions were created, the findings presented here may be the basis for a more detailed study on whether or not the assumptions made in determining a single value for the turbulent decay exponent assume too much.

CHAPTER 4

CONCLUSIONS

Direct numerical simulations of turbulent velocity fields, wall boundary conditions were applied, and the resulting velocity fields were examined using two-point correlations. This thesis initially aimed at decomposing the two-point correlations into their constitutive components to predict the statistical behavior of the velocity fields at short timescales with the wall boundary condition applied. In the course of examining this, however, a simple and elegant model was developed, for the prediction of the two-point correlations of the velocity fields after the imposition of the wall. This reflection technique accurately predicts any two-point correlation computed with wall-perpendicular velocities. More intriguing, it predicts the behavior of a non-linear quantity with a linear operation. The model, in its current state, does not accurately predict correlations computed with only wall-parallel velocities. In these situations, the correlations have less of an impact from the wall, as a free-slip boundary condition exists for the velocity parallel to the wall.

Taking another approach at solving for the wall-parallel correlations, the vorticity of the turbulent velocity fields were examined. While calculating the vorticity in the staggered mesh velocity field is relatively easy, deriving velocity from the vorticity fields was not. In this work, we were able to develop and validate a modified Biot-Savart method that can closely approximate the velocity field corresponding to a vorticity field. Using these vorticity fields, it was possible to duplicate the wall

boundary condition, and reproduce the velocity fields as they are after the wall boundary condition was imposed solely in the velocity fields. Furthermore, in decomposing the two-point correlations, into its contributions from its pre-wall velocities from either side of the wall location, it was shown that only the sub-correlations involving velocities on the proper side of the wall contribute significantly to the correlations as they are after the wall was imposed. This explains why the linear operation is sufficient.

The last major component to this thesis is the generation of new initial conditions. The generation of turbulent initial conditions is challenging to do properly, and more so to simulate real world situations. This thesis covers the method of turbulent field generation, and how it was aimed at maintaining a degree of physical realizability. Multiple initial conditions were developed, with varying turbulent Reynolds numbers. More importantly, the method for the creation of such initial conditions was developed as to allow future researchers to create their own initial conditions, for whatever area of study was needed (higher Reynolds numbers, Low Reynolds numbers, etc.)

In developing these new initial conditions in house, we can examine the decay exponent associated with decaying isotropic turbulent fields. There is a wide disparity in what the value of this exponent should be, and that is largely due to the variations in initial conditions used. While we arrive at values of the decay exponent in the expected range of values, our results lead us to a conclusion with more questions than the answers we had hoped for. The generalization of such a complex flow to one variable may not necessarily be the best way to quantify its behavior. In knowing exactly how

the initial conditions were created, and that they were made to mimic a physically realizable condition, allows for further efforts to be made to develop the theory on what the value of the decay exponent should be, or if it should be a single value at all.

REFERENCES:

1. Pope, S.B., *Turbulent flows*. 2000, Cambridge ; New York: Cambridge University Press. xxxiv, 771 p.
2. de Bruyn Kops, S.M. and J.J. Riley, *Direct numerical simulation of laboratory experiments in isotropic turbulence*. *Physics of Fluids*, 1998. **10**(9): p. 2125-2127.
3. Taylor, G.I., *Statistical theory of turbulence*. *Proceedings of the Royal Society of London Series a-Mathematical and Physical Sciences*, 1935. **151**(A873): p. 0421-0444.
4. von Kármán, T. and L. Howarth, *On the statistical theory of isotropic turbulence*. *Proceedings of the Royal Society of London Series a-Mathematical and Physical Sciences*, 1938. **164**(A917): p. 0192-0215.
5. Hallböck, M., *Development of Reynolds Stress Closures of Homogeneous Turbulence through Physical and Numerical Experiments*, in *Department of Mechanics*. 1993, Royal Institute of Technology: Stockholm.
6. Comtebel.G and S. Corrsin, *Use of a Contraction to Improve Isotropy of Grid-Generated Turbulence*. *Journal of Fluid Mechanics*, 1966. **25**: p. 657-&.
7. Perot, J.B. and S.M. de Bruyn Kops, *Modeling turbulent dissipation at low and moderate Reynolds numbers*. *Journal of Turbulence*, 2006. **7**(69): p. 1-14.
8. Saffman, P.G., *Large-Scale Structure of Homogeneous Turbulence*. *Journal of Fluid Mechanics*, 1967. **27**: p. 581-&.
9. Gadebusch, J.A., *On the Development of Self-adapting (RANS/LES) Turbulence Models for Fluid Simulation at any Mesh Resolution*, in *Mechanical and Industrial Engineering*. 2007, UMASS - Amherst: Amherst, MA. p. 105.
10. Perot, J.B., *An Analysis of the Fractional Step Method*. *Journal of Computational Physics*, 1993. **108**(1): p. 51-58.
11. Shewchuk, J.R., *An Introduction to the Conjugate Gradient Method Without the Agonizing Pain*, in *School of Computer Science*. 1994, Carnegie Mellon University: Pittsburgh, PA. p. 64.
12. Wilcox, D.C., *Basic fluid mechanics*. 2nd ed. 2000, La Cañada, Calif.: DCW Industries. xxvi, 786 p.
13. Anderson, J.D., *Computational fluid dynamics : the basics with applications*. McGraw-Hill series in mechanical engineering. 1995, New York: McGraw-Hill. xxiv, 547 p.
14. Lecuyer, P., *Efficient and Portable Combined Random Number Generators*. *Communications of the Acm*, 1988. **31**(6): p. 742-&.
15. Bratley, P., Fox, B.L., and Schrage, L. E., *A Guide to Simulation by Bratley, P., Fox, B.L., and Schrage, L. E.* *Simulation*, 1987. **42**(6): p. 294-294.
16. Yokota, R., T.K. Sheel, and S. Obi, *Calculation of isotropic turbulence using a pure Lagrangian vortex method*. *Journal of Computational Physics*, 2007. **226**(2): p. 1589-1606.

17. Katz, J. and A. Plotkin, *Low speed aerodynamics*. 2nd ed. Cambridge aerospace series ; 13. 2001, Cambridge, UK ; New York: Cambridge University Press. xvi, 613 p.